JGR Earth Surface

RESEARCH ARTICLE
10.1029/2018JF004848

Key Points:
- Four composite debris-on-ice thermal stress models are tested and compared to observations
- Elastic component of rheological model is necessary for short timescale of diurnal thermal stresses
- Diurnal thermal stress is important weathering factor unless ice is shielded by a 0.5-m-thick debris mantle

Supporting Information:
- Supporting Information S1
- Video S1
- Video S2
- Video S3
- Video S4

Correspondence to:
E. A. Podolskiy,
evgeniy.podolskiy@gmail.com

Citation:
Podolskiy, E. A., Fujita, K., Sunako, S., & Sato, Y. (2019). Viscoelastic modeling of nocturnal thermal fracturing in a Himalayan debris-covered glacier. *Journal of Geophysical Research: Earth Surface*, *124*, 1485–1515. https://doi.org/10.1029/2018JF004848

Received 27 AUG 2018
Accepted 3 MAY 2019
Accepted article online 8 MAY 2019
Published online 17 JUN 2019
Corrected 28 JUN 2019

This article was corrected on 28 JUN 2019. See the end of the full text for details.

Viscoelastic Modeling of Nocturnal Thermal Fracturing in a Himalayan Debris-Covered Glacier

Evgeny A. Podolskiy[1,2], Koji Fujita[3], Sojiro Sunako[3], and Yota Sato[3]

[1]Arctic Research Center, Hokkaido University, Sapporo, Japan, [2]Global Station for Arctic Research, Global Institution for Collaborative Research and Education, Hokkaido University, Sapporo, Japan, [3]Graduate School of Environmental Studies, Nagoya University, Nagoya, Japan

Abstract Recent observations suggest that the nocturnal thermal fracturing of ice occurs at relatively warm temperatures (above −15 °C) at a high-altitude Himalayan glacier system unless the ice is shielded by a debris mantle. Here we estimate the stresses induced by diurnal temperature variations using viscous, elastic, and two viscoelastic models, and various thicknesses of the debris mantle. Only the elastic and visco-elastic models are in agreement with the observations. The timing and amplitudes of the stresses in the upper 15 cm of the glacier are different among the models despite the ability of each approach to predict a diurnal increase in tension exceeding the critical threshold proposed for crevasse formation. For example, the elastic stress is several times larger than the viscous stress at the ice surface (650 vs. 250 kPa) and reaches its peak up to 5–6 hr later in the night. The time lag is in line with the seismic records, suggesting that the viscous model is not appropriate. Furthermore, a debris layer of ≥50 cm in thickness suppresses the diurnal fluctuations in thermal stress and therefore protects the ice from mechanical damage. We suggest that high-amplitude diurnal cooling and weak ice properties due to weathering are essential factors that influence thermal fracturing in the Himalayan environment. The ongoing expansion of seismic networks into cryospheric regions, which will be capable of detecting local thermal-contraction-induced cracks, in combination with the fact that such cracks can erode and weaken the ice, and thereby serve as meltwater and heat channels, warrants further research to better understand these near-surface processes and to monitor ice properties.

Plain Language Summary Thermal fracturing is an important erosion process on the icy surfaces of solar system bodies, including Earth, Mars, and comets. However, the exact timing of this thermal fracturing process is poorly constrained, despite the need for this information to validate models, and its importance in the weathering of glacial ice is largely unknown and often overlooked. Recent seismic observations revealed nocturnal thermal fracturing of a high-altitude Himalayan debris-covered glacier. These observations in Nepal suggested that glacial ice bursted with icequakes as temperature decreased unless ice was protected with a thick debris cover. In this study we consider four different numerical approaches to describe material behaviour of ice under thermal stress in order to find out how debris modulates stresses and which method agrees with the experimental evidence. We numerically estimate thermal stress conditions near the surface of a glacier with and without debris and find that a half-of-a-meter-thick debris is sufficient to protect ice from mechanical damage induced by diurnal variation of temperature. Furthermore, our study suggests that thermal stress could be an important factor for weathering of exposed ice and that this process needs more attention since it is possible that new cracks can facilitate ablation.

1. Introduction

Crustal thermoelastic strain due to air temperature variations is known to have the largest nontectonic effect on strainmeter and global positioning system records (Berger, 1975; Prawirodirdjo et al., 2006) and can lead to seismic velocity changes (Richter et al., 2014). Diurnal and annual temperature variations, in rock and ice, attenuate within the upper 1 and 20 m of the material, respectively (Ben-Zion & Leary, 1986; Sanderson, 1978). Thermal strains induce near-surface thermal stresses, which are recognized as an important agent in various processes. For example, the thermal stress in ice cover is important for dam design (Petrich et al., 2015), can cause large-scale fractures in sea ice (Bazant, 1992; Evans & Untersteiner, 1971; Lewis, 1994; Xie & Farmer, 1991) and lake ice (Carmichael et al., 2012), is responsible for polygon formation in permafrost on Earth and Mars (Lachenbruch, 1962; Levy et al., 2009; Mellon, 1997; O'Neill & Christiansen, 2018), and is suggested to be an important erosion process on cometary surfaces and the Moon (e.g., Attree et al., 2017). Sanderson (1978) conducted analytic investigations of thermal stresses near glacial surfaces and concluded that (i) in the upper 3 m of the ice, thermal stresses dominate those originating from the overburden pressure and from the gross deformation; (ii) tensile fracture cannot develop in pure ice due to its high tensile strength, unless assisted by stress concentrations at heterogeneities; and (iii) such fractures are more likely to form in weaker firn and snow.

A recent review of crevasse and crack formation does not mention the possibility of ice thermal cracking (Colgan et al., 2016). Nevertheless, the so-called "critical stress" of pure ice—the critical tensile stress threshold of 100–400 kPa associated with the formation of new crevasses (Colgan et al., 2016)—is lower than the tensile fracture strength by ∼1,000 kPa (Petrovic, 2003). Similarly, Nishio (1983) estimated that fracturing in dense glazed snow occurs at 40 kPa, which is lower than the tensile fracture strength of hard snow or firn (∼300 kPa). These observations confirm the idea that the local mechanical properties of ice and snow, in combination with the presence of defects, may lead to fracturing at relatively small stresses (e.g., thermal stresses; Lewis, 1993; Petrich et al., 2015) that are only ∼15% of the material strength.

Coacoustic thermally induced fractures, generally in the firn and snow cover of glaciers, have previously been reported for very cold temperatures; for example, −40 °C (Nansen, 1897), below −25 °C (Nishio, 1983), and below −30 °C (Sanderson, 1978). Marchant et al. (2002) observed thermal cracks on the surface of a stagnant glacier buried under a debris layer (0.38–0.7 m thick) in the Dry Valleys, Antarctica (mean annual surface temperature of approximately −34 °C). These examples suggest that significant thermal cracking only occurs when the surface temperatures are below −30 °C. Major ice-wedge cracking in permafrost preferentially occurs when the surface temperature is below −20 °C, with these warmer conditions potentially corresponding to weaker wedge ice, which is known to contain sediment inclusions, bubbles, and foliations (Matsuoka et al., 2018; O'Neill & Christiansen, 2018). Acoustic ambient noise observed beneath the shore-fast ice in the Arctic was found to be controlled by the air temperature (Milne et al., 1967). Ice cracking was observed when the temperature decreased to the −20 to −14 °C range. Sea ice thermal-contraction cracking at such relatively modest temperatures might be due to thermal bending, which intensifies the stress (Bazant, 1992). Similarly, the thermal bending of a frozen lid overlying slushy ice/water was associated with seismicity on an ice shelf in Antarctica (MacAyeal et al., 2019). To our knowledge, with the exception of a study in Tibet by Zhang et al. (2019), the thermal contraction cracking of glacier ice has not been observed at temperate alpine glaciers (Neave & Savage, 1970) or in the ablation zone of the Greenland Ice Sheet, where dynamic stresses and hydrofracturing are dominant (Röösli et al., 2014).

However, observations of intense nocturnal icequake activity at a high-altitude Himalayan debris-covered glacier system by Podolskiy et al. (2018b) suggest that the thermomechanical state of the near-surface ice easily reaches fracture conditions unless the ice is insulated by a thick debris mantle. Therefore, the mechanisms influencing such unique behavior, which has primarily been studied in snow and sea ice conditions at significantly colder temperatures in polar regions, should be thoroughly investigated. This is particularly important because it may correspond to a strong and largely overlooked weathering agent of glacier ice. No focused analysis of the relationship between thermal stress and ice fracturing has been made on debris-covered glaciers to date, despite recent interest in the role of debris on the mass balance of glaciers and snow patches (e.g., Fujita & Sakai, 2014; Podolskiy et al., 2015). The main possible factors that lead to the processes observed by Podolskiy et al. (2018b) are (1) the elastic response of the ice, (2) high diurnal temperature fluctuations, and (3) weak ice with high stress at heterogeneities.

A comprehensive literature search suggests that a study of snowquakes in East Antarctica by Nishio (1983) is the most detailed in situ cryospheric investigation of thermally induced cracks to date. The author conducted a comprehensive analysis of snow temperature, crack-width variations, and snowquake seismic monitoring, and observed the following:

1. thermal cracks were produced due to increased tensile stresses during snow contraction in response to decreasing temperatures;
2. snowquakes were not observed at temperatures above −23 °C;
3. snowquakes usually occurred during a rapid drop in surface temperature (1–2 °C/hr at approximately −25 °C and as low as 0.5 °C/hr at −50 °C); and
4. the number of snowquakes increased with increasing thermal strain.

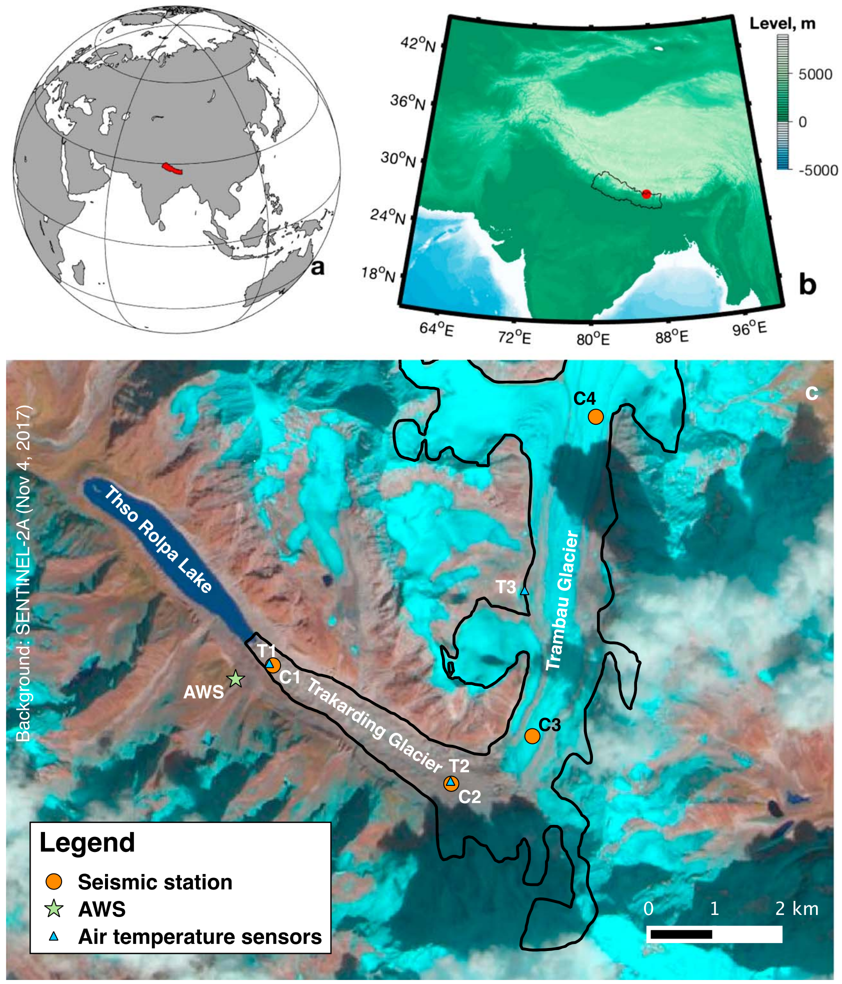

Figure 1. The study site in the Trakarding-Trambau Glacier system, Nepal Himalaya. (a) General location of the Nepal Himalaya. (b) Location of the Trakarding-Trambau Glacier system (red circle), relative to the Nepal Himalaya. (c) Observational network layout across the Trakarding-Trambau Glacier system (background SENTINEL-2A satellite image acquired on 4 November 2017; glaciers' outline is adopted from Nuimura et al., 2015). AWS = autonomous weather station.

Here we present a composite model of thermal strain and stress in ice that possesses a debris mantle of varying thickness, to assess the above-mentioned processes that best explain the in situ observed behavior reported by Podolskiy et al. (2018b). We further demonstrate that ignoring ice elasticity (e.g., Sanderson, 1978) results in errors, as it leads to an underestimate of the stress magnitude and an incorrect estimate of the timing of fracturing.

2. Materials and Methods

2.1. Experiment Summary

Trakarding-Trambau Glacier system is located in Eastern Nepal, between 4,520- and 6,690-m elevation. It covers an area of about 32 km^2 and has a length of ~17 km; the ice thickness ranges between approximately 75 and 280 m at the lower and upper parts of the system, respectively. The mean ice flow speed is only ~15 m/a. A detailed explanation of the temporary observational network deployed across the glacier system can be found in Podolskiy et al. (2018b). A comprehensive description of the study area, highlighting the importance of glaciological monitoring in this rapidly changing region near Mount Everest, is also available in Podolskiy et al. (2018b, and references within). An overview map of the installed instruments is presented in Figure 1. The seismic stations were in operation between 25 October and 8 November 2017, with a given seismic station recording for between 4 and 14 days (at altitudes between 4,594 and 5,555 m above sea level, a.s.l.). Two stations were located on the debris-covered area (C1 and C2), and another two on the debris-free

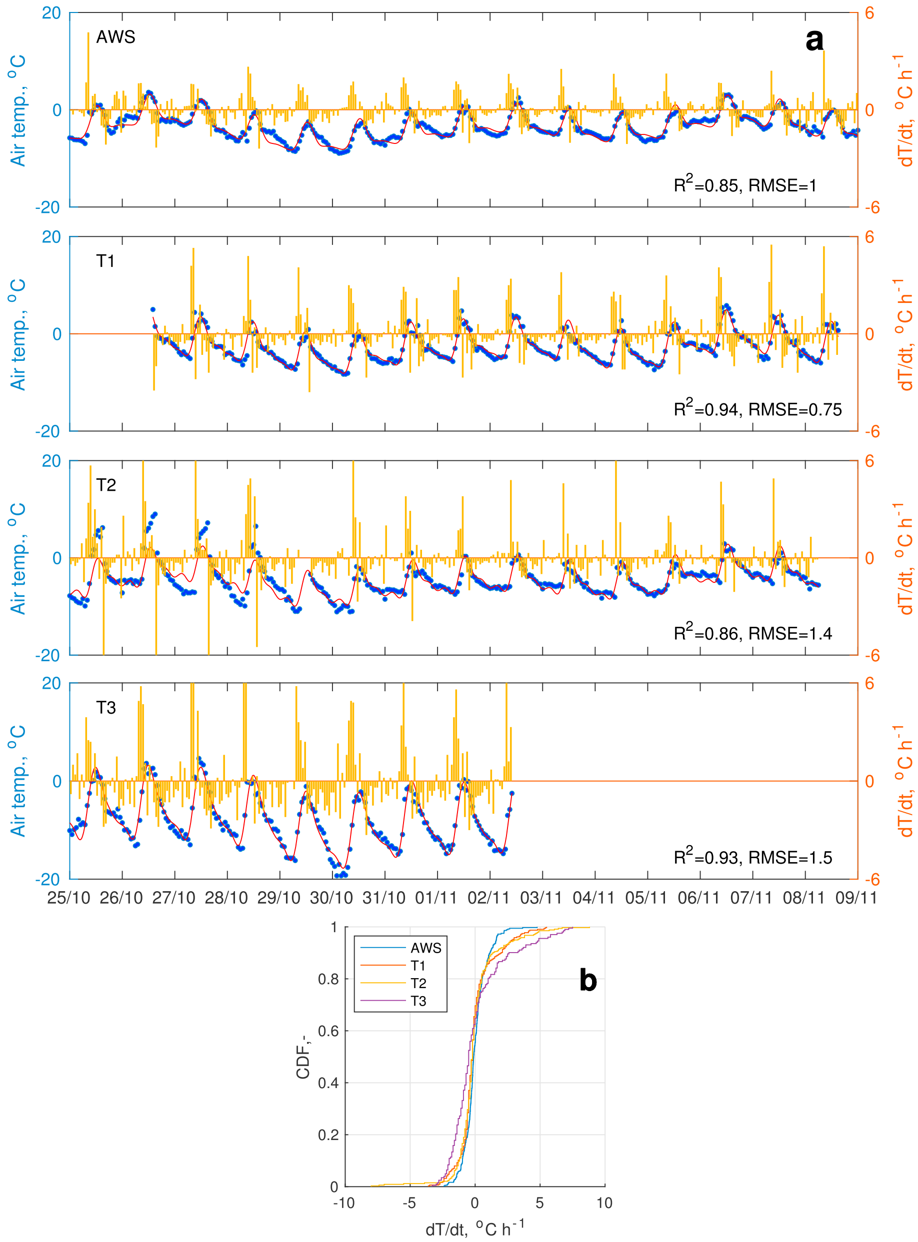

Figure 2. (a) Surface air temperature measurements (blue dots) at the four locations along the Trakarding-Trambau Glacier system, with their corresponding rates of change (yellow bars). The red curves are the best fits using an eight-term sum-of-sines model (the corresponding goodness-of-fit is expressed in each subplot as R^2 and RMSE). (b) Empirical cumulative distribution functions (CDFs) of the rates of temperature change ($\mathrm{d}T/\mathrm{d}t$). AWS = autonomous weather station; RMSE = root-mean-square error.

area of the glacier (C3 and C4). The stations in similar areas recorded ambient seismic noise with similar characteristics. For example, C1 and C2 recorded less energy at high frequencies (>2 Hz), while C3 and C4 detected significant energy at these higher frequencies. Furthermore, stations C2, C3, and C4 all show comparable temporal variations in seismic noise, displaying elevated noise levels at night, whereas station C1, which was located over the thickest debris mantle (65 vs. 23 cm at C2), recorded elevated noise levels in the afternoon. These observations suggest that the thickness of the debris mantle has a major influence on the observed glacier seismicity, which the present study aims to elucidate, with a particular emphasis on exploring the constitutive behavior of ice in order to explain the observed behavior, and the thickness of debris mantle that is sufficient to protect the ice from contraction fracturing in a given environmental setting.

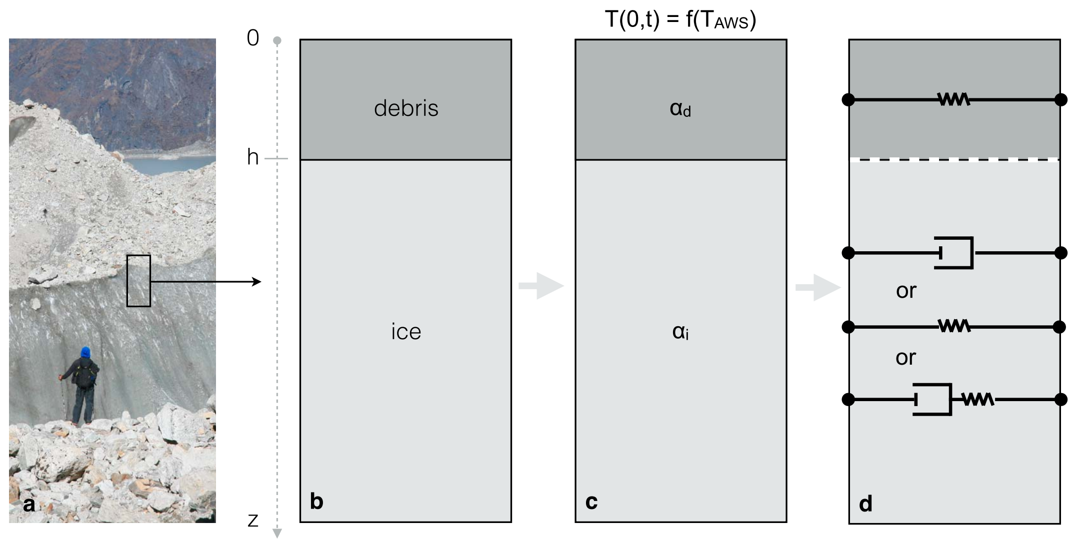

Figure 3. (a) Photograph of an ice cliff in the central section of Trakarding Glacier (taken between sites C1 and C2 on 8 November 2017) compared to a schematic overview of the composite debris-mantle-ice model, which is consisting of two layers. (b) One-dimensional geometry. (c) Heat-conduction model. (d) Rheological models subjected to thermal stress (with a spring representing elasticity and a dashpot representing viscous relaxation).

This in situ experiment presents an interesting test case for validating the existing theory on ice fracture and crevasse formation with the ability to compare the data against two different approaches to ice constitutive behaviour: that is, with or without elasticity (e.g., Attree et al., 2017; Sanderson, 1978; Zhang et al., 2019).

Surprisingly, little appears to be known of the thermal stresses in glacial ice, mechanical and crystalline properties of near-surface ice, or microcrack statistics and dynamics from an observational perspective, which makes it premature to base this study on fracture mechanics instead of strength theory. We therefore first calculate the stresses involved, assuming the ice does not fracture.

2.2. Air Temperature

We provide a brief description of the surface air temperature measurements, which were conducted at the autonomous weather station (AWS, 4,805 m a.s.l.), near seismic stations T1 (4,591 m a.s.l.), T2 (4,767 m a.s.l.), and at site T3 (5,390 m a.s.l.) in Figure 2, since the key analysis presented here concerns surface air temperature.

The mean air temperature during the campaign was approximately −2.8 °C (AWS). Interestingly, the air temperature was dropping more than 50% of the time during the campaign (between 55% and 72% at AWS and T3, respectively). However, diurnal warming occurred at larger absolute rates. The mean rate of cooling was between −1.2 and −0.6 °C/hr, and the mean rate of warming was between +0.7 and +2.1 °C/hr, depending on the site. Furthermore, the highest rates of cooling at the Trakarding-Trambau Glacier system (from −2.4 down to −3.9 °C/hr) were higher than those usually associated with snowquakes (Nishio, 1983). We also observed that the absolute value of dT/dt at its daily maximum could be even higher (from +4.7 up to +6.7 °C/hr), which may imply thermal expansion of the debris mantle.

However, we note that the large temperature changes of approximately −8.0 and +8.8 °C/hr at site T2 could be instrumental outliers, as these extreme rates were no longer recorded after a maintenance visit around noon on October 29 (seen as a short data gap in Figure 2). The exaggerated gradients observed at site T3 may also be instrumental outliers. More detailed information on the presented temperature series and how we circumvent any potential biased measurements are presented in Appendix A.

3. Thermal Stress Model

The numerical experiments presented here employ a composite model, which consists of a debris mantle over an ice half-space (Figure 3). We evaluate the effects of debris on the magnitude of strain and stress in the ice using the temperature at the bottom of the debris layer as an input for the in-ice temperature and see how the modeled strains and stresses compare with threshold values in the literature and with the seismic

Table 1
Description of the Variables Used and Discussed in This Study

Parameter	Symbol, Unit	Value or Equation	Note or reference
Mean annual air temperature	T_o, °C	−0.14 at AWS, −0.35 at T1, −0.57 at T2, −4.26 at T3	T1 was incomplete, take mean (AWS, T2)
Density of ice	ρ_i, kg/m^3	917	
Density of debris	ρ_d, kg/m^3	1,408 near C1, 1,440 near C2	measured in October 2017 (Reid & Brock, 2010: 250 or 1496)
Thermal conductivity of ice	k_{Ti}, W·m^{-1}·K^{-1}	$2.1\times10^{-2}+4.2\times10^{-4}\rho_i+2.2\times10^{-9}\rho_i^3$	Cuffey and Paterson (2010)
Thermal conductivity of debris	k_{Td}, W·m^{-1}·K^{-1}	0.94 near C1, 0.47 near C2	measured in October 2017 (Reid & Brock, 2010: 0.35 or 0.94)
Specific heat capacity of ice	c_i, J·kg^{-1}·K^{-1}	152.5 + 7.122 (T_o + 273.15)	Cuffey and Paterson (2010)
Specific heat capacity of debris	c_d, J·kg^{-1}·K^{-1}	750	Nicholson and Benn (2006)
Young's modulus of debris mantle	E_d, Pa	5×10^9	
Young's modulus of ice	E_I, Pa	4×10^9	Petrich et al. (2015)
Poisson's ratio of debris	ν_d, -	0.25	
Poisson's ratio of ice	ν_I, -	0.31	
Linear coeff. of expansion of ice	a_I, °C^{-1}	53 ×10^{-6}	Sanderson (1978)
Linear coeff. of expansion of debris	a_d, °C^{-1}	6×10^{-6}	
Tensile strength of ice	σ_I, Pa	1.43 ×10^6 Pa	Petrovic (2003)
Tensile strength of firn	σ_f, Pa	0.3 ×10^6 Pa	Nishio (1983)
Thermal diffusivity of ice	α_I, m^2/s	$k_{Ti}/(\rho_i c_i)$	
Thermal diffusivity of debris	α_d, m^2/s	$k_{Td}/(\rho_d c_d)$	
Gas constant	R, J·mol^{-1}·K^{-1}	8.3144598	
High-temperature (above −10 °C) activation energy for creep	Q^+, J/mol	150×10^3	Cuffey and Paterson (2010)
Creep exponent	n, -	3	Cuffey and Paterson (2010)
Prefactor for the creep parameter A	A_o, s^{-1} Pa^{-n}	1.3368×10^5 for n=3, Q^+ = 150k J/mol at −2 °C	Cuffey and Paterson (2010)

experiment. This approach is inspired by the composite model of thermoelastic strain by Ben-Zion and Leary (1986) that has been adopted as a simplified representation of unconsolidated material covering an ice half-space. We describe the model in the following subsections, and the model parameters are summarized in Table 1.

3.1. Heat Conduction in Two-Layer System

The full one-dimensional heat-diffusion equation for a vertically heterogeneous medium with depth-dependent properties is

$$c(z)\rho(z)\frac{\partial T(z,t)}{\partial t}=\frac{\partial}{\partial z}\left(k(z)\frac{\partial T(z,t)}{\partial z}\right), \tag{1}$$

where ρ is the density, c is the specific heat capacity, and k is the thermal conductivity (Ferrari, 2018). In case of a homogeneous layer with constant k, c, and ρ (i.e., $\frac{\partial}{\partial z}=0$), the heat-diffusion equation can be simplified and solved analytically as shown below. Furthermore, for a two-layer medium, a system of heat-diffusion equations in their reduced form can be used to describe the heat transport through each layer with particular thermophysical properties (González de la Cruz & Gurevich, 1995). Accordingly, surface-temperature-induced variations at the bottom of the upper layer can be treated as the surface boundary condition for the lower layer. To our knowledge, such approach yielded a good agreement between modeled and observed thermoelastic strains in the crust (e.g., Ben-Zion & Leary, 1986; Prawirodirdjo et al., 2006). However, in order to further validate this approach, with the main concern been associated with conservation of energy, we compare it to a numerical solution obtained through the Finite Difference Method (FDM) as detailed in Appendix B.

Thermal diffusion of the air surface temperature into the upper vertically homogeneous layer of the glacier is analyzed by solving the heat conduction equation with a cyclic variation in temperature as the surface boundary condition:

$$\frac{\partial T(z,t)}{\partial t} = \alpha \frac{\partial^2 T(z,t)}{\partial z^2}$$

$$T(0,t) = T_o + A_t \cos(\omega t), \tag{2}$$

which yields

$$T(z,t) = T_o + A_t \exp(-z\sqrt{\omega/(2\alpha)}) \times \cos(\omega t - z\sqrt{\omega/(2\alpha)}), \tag{3}$$

where z is the depth, which increases from the surface downward, T_o is the mean annual surface temperature or reference temperature (°C), A_t is the diurnal temperature amplitude (not to be confused with diurnal peak-to-peak fluctuation), ω is the angular frequency (e.g., $\omega = 2\pi$ is 1 cycle per day), and α denotes the thermal diffusivity of the upper-layer material m ($m = $ [I, d] for ice and debris, respectively; $\alpha = \frac{k_m}{c_m p_m}$; see Table 1 for details).

Any surface boundary condition that satisfies the Dirichlet criterion and can be expanded as a Fourier series or closely related series will have a solution, as the corresponding solutions are superposable (Sanderson, 1978). The sum-of-sines series expansion for the variation in surface air temperature in our study is

$$T(0,t) = \sum_{r=1}^{8} A_r \sin(\omega_r t + \phi_r), \tag{4}$$

where the index r is a number of a particular harmonic with its own amplitude (A), frequency (ω), and phase (ϕ). See Appendix A for more details on the preprocessing of the input air temperatures employed in the model.

The corresponding ice temperature beneath a debris layer with thickness h ($z \geq h$) is further attenuated and lagged by the debris layer and therefore equivalent to

$$T(z,t) = \sum_{r=1}^{8} A_r \exp(-(z-h)\sqrt{\omega_r/(2\alpha_I)}) \exp(-h\sqrt{\omega_r/(2\alpha_d)}) \times$$

$$\cos(\omega_r t - (z-h)\sqrt{\omega_r/(2\alpha_I)} - h\sqrt{\omega_r/(2\alpha_d)} + \phi_r), \tag{5}$$

where α_I is the thermal diffusivity of ice and α_d is the thermal diffusivity of the debris layer. The latter is relatively well constrained by in situ thermal conductivity and density measurements made within tens of meters of sites C1 and C2 during the campaign (Table 1). Please note that the case where $h = 0$ in equation (5) corresponds to the debris-free case.

The above heat conduction equations allow us assess how the temperature variations are attenuated and lagged with depth, with the attenuation being particularly strong for high-frequency (e.g., daily) fluctuations. However, one of the physical limitations of applying these classical formulas to ice occurs when the absolute value of the diurnal surface air temperature amplitude is higher than the absolute value of the mean temperature. In other words, the ice temperature cannot rise above 0 °C when the surface temperature rises above the melting point of ice, and all excess heat energy goes into melting. We prohibit the temperature to rise above 0 °C for this rare, but occasionally occurring condition, and obtain the time derivative of $T(z,t)$ numerically.

3.2. Constitutive Behavior of the Debris Mantle

It is reasonable to adopt the same approach as proposed by Ben-Zion and Leary (1986) in our analysis, and to consider the debris mantle as a layer that is elastically decoupled from the underlying ice (Figure 3). This implies that the strains and stresses in the debris mantle have no influence on our calculations for ice. On the one hand, such approach permits us to omit any stress calculations for the debris mantle. On the other hand, it gives us liberty to use a simplified constitutive relationship (e.g., by disregarding the nonlinear behavior of granular solids; Andreotti et al., 2013, which could be relevant to some degree to the debris mantle). Here we choose the latter opportunity for the following two reasons: (i) it allows us to keep the overall integrity of

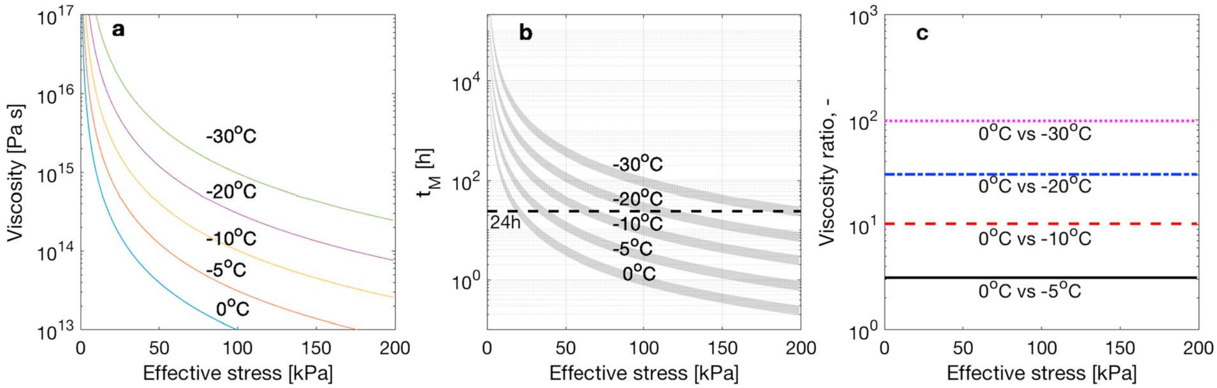

Figure 4. (a) Effective viscosity of ice as a function of effective stress (after Greve & Blatter, 2009). (b) The corresponding Maxwell viscoelastic relaxation time (with G from 2.3 to 3.6 GPa). (c) Relative change in viscosity with decreasing temperature compared with the viscosity at 0 °C (η_X/η_0).

our modeling framework and continuity of all related figures and (ii) it permits to compare debris stresses with some secondary features of the observed seismicity (as detailed below in section 3.4). Therefore, we assume a linear isotropic thermoelasticity of the debris mantle, which comprises a mixture of rocks, as its effective, macroscopic constitutive behavior (Berger, 1975; Mellon, 1997):

$$\epsilon_{ij}^{E} = \frac{1+\nu_d}{E_d}\sigma_{ij} - \frac{\nu_d}{E_d}(\sigma_{kk})\delta_{ij} = a_d \Delta T \delta_{ij}, \tag{6}$$

where the superscript E indicates the elastic component, the subscripts indicate the tensor components, ϵ_{ij} is the strain tensor, ν_d is Poisson's ratio (with a typical value of 0.25 for rocks), σ_{ij} is the stress tensor, E_d is the effective Young's modulus of debris, δ_{ij} is the Kronecker delta, a_d is the effective linear coefficient of expansion of the debris, and ΔT is the difference between the instantaneous and reference temperatures corresponding to a no-stress state ($\int_0^x \frac{\mathrm{d}T(z,t)}{\mathrm{d}t}\mathrm{d}t$, where x is the length of the time period considered). (The associated "drift" of stresses due to a cumulative nature of the latter operation will be discussed in section 4.3 and dealt with by filtering.) The two parameters E_d and a_d are poorly known, especially for such a granulometrically diverse mixture of rock. The key feature of granular media is that it is significantly softer than the material constituting its particles (e.g., Andreotti et al., 2013). Therefore, we assume $E_d = 5$ GPa, which is higher than that for normally consolidated clay (2 GPa) but lower than that for overconsolidated boulder clay (15 GPa), and $a_d = 6\times10^{-6}$ ° C^{-1}, which is commonly reported for rocks (Table 1).

For a plate in a "plane stress" state (with $\sigma = \sigma_{11} = \sigma_{22}$, $\sigma_{33} = 0$, and $\epsilon = \epsilon_{11} = \epsilon_{22}$), the stress tensor in equation (6) corresponds to

$$\sigma_d = \frac{E_d}{1-\nu_d}\epsilon^E = \frac{E_d}{1-\nu_d}\Delta T a_d. \tag{7}$$

We note that the "plane stress" assumption is appropriate here since we consider an infinite and thin plate, such as a debris mantle or the upper skin of a half-space, where the material cannot expand or contract (e.g., Mellon, 1997). Problems involving a "thicker" continuum and laterally heterogeneous temperature field generally employ the "plane strain" assumption (Berger, 1975; Ben-Zion & Leary, 1986).

3.3. Constitutive Behaviour of the Ice Half-Space

The rheological model of ice should include all the key ice properties for the short diurnal timescale considered here, namely, elasticity, creep relaxation, and temperature dependence of the creep rate. Sanderson (1978) treated ice as a non-Newtonian fluid with a generalized Glen-Nye rheology when he calculated the thermal stresses in near-surface glacial ice. Contrary to more recent studies on Martian permafrost, comets (e.g., Attree et al., 2017; Mellon, 1997), and lake ice (Petrich et al., 2015), Sanderson (1978) omitted elasticity since some experimental evidence suggested that "ice responds elastically only over a time scale of 5 to 10 s." We argue that this assumption is invalid and may lead to incorrect stress calculations. Furthermore, Petrich et al. (2015) demonstrated that the measured thermal stresses in the ice cover of a reservoir are well reproduced using a viscoelastic rheology.

According to Greve and Blatter (2009), the effective viscosity approaches infinity near the glacier surface, compared with deeper parts of the glacier, which accommodates most of the shear strain of the flow ($\eta = \frac{1}{2A(T')\sigma_e^2}$, where η is the effective viscosity, A is the creep-related parameter, and σ_e is the effective stress; see equation 4.22 in Greve & Blatter, 2009, for further details). For example, a stress drop from 100 to 20 kPa corresponds to an order of magnitude increase in viscosity (Figure 4). This stress drop impacts the so-called Maxwell relaxation time, t_M, near the glacier surface, which decays at a characteristic time equal to $\frac{\eta}{G}$, where G is the shear modulus of ice (~3 GPa). The Maxwell relaxation time represents a timescale that separates the elastic and viscous responses, with a shorter time corresponding to a faster stress relaxation (Podolskiy & Walter, 2016), and t_M being significantly higher near the glacier surface than at depth. For example, when using the effective viscosity computed according to Greve and Blatter (2009) for soft ice (0 °C), the corresponding Maxwell relaxation time increases inversely with depth from ~1 to ~24 hr at stresses of ~100 and 20 kPa, respectively (Figure 4). Colder ice (−10 °C) leads to an order of magnitude increase in t_M. This strongly suggests that elastic behavior can dominate the viscous response of ice over timescales that capture diurnal variations in air temperature. Here we test three rheological models to support this argument: thermoviscous, thermoelastic, and thermoviscoelastic (Figure 3) and observe which best explains the seismic observations.

3.3.1. Thermoviscous Model

We follow Sanderson (1978) in calculating stresses for the thermoviscous model, which adopted the Glen-Nye isotropic flow law:

$$\dot{\epsilon_{ij}}^V = A_o \exp\left(-\frac{Q}{RT}\right)\tau_E^{n-1}\tau_{ij}, \tag{8}$$

where the superscript V indicates the viscous component, $\dot{\epsilon_{ij}}^V$ is the strain rate tensor, A_o is a prefactor of the creep parameter, Q is the temperature-dependent activation energy for creep, R is the gas constant, T is the temperature relative to the pressure melting point (in K; Greve & Blatter, 2009), τ_E is the effective stress (with a creep exponent $n = 3$ as the most widely accepted preference over the range of 1–4.7; e.g., Attree et al., 2017; Cuffey & Paterson, 2010; Petrich et al., 2015), and τ_{ij} is the stress deviator ($\tau_{ij} = \sigma_{ij} - \frac{1}{3}\sigma_{kk}\delta_{ij}$). Sanderson (1978) assumed an infinite plain geometry to derive the thermal stresses, where the thermal volumetric changes were laterally restrained (a “rigid box”), employing only the stresses necessary to resist motion to address the observed expansion or contraction. This allows the incompressibility of ice to be maintained as a basis of the Glen-Nye flow law. The corresponding effective strain rate of a material subject to the temperature-time gradient is equal to

$$\dot{\epsilon_{ij}}^T = \left(-a_I\frac{\partial T}{\partial t}\right)\delta_{ij}, \tag{9}$$

where a_I is the effective linear coefficient of expansion of ice and $\frac{\partial T}{\partial t}$ is the main modulator of the “volumetric” changes in the ice mass, which can be readily obtained either numerically of via differentiation of equation (5). Sanderson (1978) chose expanding coordinates to formulate the problem of a thermally fluctuating region attached to a continuum that creeps longitudinally at a gross strain rate, $\dot{\epsilon_1}$. The formulation was developed without any treatment of the shear stresses, as they were negligible near the surface in the vertical plane and could be eliminated by aligning the spatial frame of analysis with the principal axes in the horizontal plane (the third principal axis, in the vertical direction, was chosen perpendicular to the glacier surface).

Equations 8 and 18 in Sanderson (1978) are combined to determine the resultant horizontal total stresses ($\tau = \tau_{11} = \tau_{22}$) as follows:

$$\tau = \left(\frac{(\dot{\epsilon_1} - a_I\frac{\partial T}{\partial t})\exp[\frac{Q}{RT}]}{3A_o}\right)^{\frac{1}{3}} \tag{10}$$

where the “3” in the denominator corresponds to the assumption that $\dot{\epsilon_1} = \dot{\epsilon_2}$, which simplifies the equations and accounts for the fact that the transversal strain component is poorly known at the Trambau-Trakarding Glacier system (see Appendix C). Inspection of equation (10) suggests that a decrease in temperature and a large negative temperature gradient correspond to a higher tensional stress, while $\dot{\epsilon_1}$ corresponds to the background stress.

Sanderson (1978) demonstrated that the significant longitudinal strain rate of ice streams (on the order of 10^{-3} a^{-1}) had little effect on the thermal stress estimation. The slow-moving Trakarding-Trambau Glacier system, which decelerates from ~27 m/a at its upglacier extent to 3 m/a near the terminus (Appendix C), yields a corresponding representative strain rate of $\dot{\epsilon_1} = -2.6 \times 10^{-3}$ $a^{-1} = -0.8 \times 10^{-10}$ s^{-1}, with the minus sign denoting compression. According to equation (10), the associated "background" compressive stress is only approximately −25 kPa.

Finally, we note that when we change the constant T (as it is assumed by Sanderson, 1978) to a variable $f(t)$, the temperature increase will correspond to a faster viscous relaxation of accumulated stress, and vice versa, where the temperature decrease indicates a slower stress relaxation. This asymmetry means that the stresses during warm temperatures will be lower than those during cold temperatures. Petrich et al. (2015) reported that this temperature dependence of the creep rate is crucial for reproducing thermal stresses measurements in warm ice (above −10 °C).

3.3.2. Thermoelastic Model

The purely elastic behavior of ice is described and treated in exactly the same form as that for debris; that is,

$$\sigma_I = \frac{E_I}{1 - \nu_I}\epsilon^E = \frac{E_I}{1 - \nu_I}\Delta T a_I, \tag{11}$$

with all the corresponding ice parameters listed in Table 1 or discussed below. It is clear from equation (11) that the thermoelastic stress is directly proportional to the chosen value of Young's modulus. It is expected that the effective stiffness of the near-surface ice may be significantly lower (e.g., 4 GPa) than the commonly assumed 9 GPa for pure ice, as a result of weathering, relatively low strain rates, and a high surface temperature (see Appendix D for details).

3.3.3. Thermoviscoelastic Models

Several viscoelastic models were proposed to describe ice, including a Maxwell material, a Rivlin-Ericksen material, and an approach inspired by Fiber-Bundle models (e.g., Christmann et al., 2019; Keller & Hutter, 2014; Riesen et al., 2010). Here, we add an elastic term to the Maxwellian thermoviscoelastic model (e.g., Attree et al., 2017; Mellon, 1997) and omit the gross strain rate for simplicity, based on our previous arguments that they are negligible. The model assumes ice as a Maxwellian viscoelastic solid with its elastic and viscous behaviors acting in series (Mellon, 1997); this is reasonable since a "series" approach allows a purely viscous response to infinite strain. Specifically, for a total strain rate, $\dot{\epsilon_{ij}}$, which is equal to 0 (i.e., the null divergence of the velocity field for incompressible flow), the governing equation can be broken into its elastic (E), viscous (V), and thermal (T) components:

$$\dot{\epsilon_{ij}} = 0 = \dot{\epsilon_{ij}}^E + \dot{\epsilon_{ij}}^V + \dot{\epsilon_{ij}}^T$$

or

$$0 = \frac{1 - \nu_I}{E_I}\dot{\tau} + FA_o exp[-\frac{Q}{RT}]\tau^3 - a_I\frac{\partial T}{\partial t} \tag{12}$$

Here $\dot{\epsilon_{ij}}^V$ (with a factor $F = 3$) is adopted from Sanderson (1978) for consistency, instead of employing the reduced-creep form presented by Mellon (1997) for permafrost (with a factor $F = 2^{-n}$). The Mellon (1997) approach leads to viscous stresses that are larger than those calculated via the Sanderson (1978) approach by a factor of $6^{\frac{1}{3}}$ (≈1.8). This discrepancy arises in part because Mellon (1997) introduced a correction factor, whereas Sanderson (1978) provided a full mathematically rigid solution, which we find more convincing and appropriate for our application. See Mellon (1997) and Sanderson (1978) for details of the differences between these two approaches.

Finally, we also compute the thermoviscoelastic stresses using an empirical model developed to estimate horizontal thermal stresses in the ice cover of a reservoir (Petrich et al., 2015):

$$\dot{\tau} = (1 - CT)\left[A\frac{\partial T}{\partial t} - \text{sign}(\tau)B\left(\frac{T_1}{T_1 - T}\right)^m\left(\frac{\tau}{\tau_0}\right)^n\right], \tag{13}$$

where $A = 131 \times 10^3$ Pa/°C and $B = 27 \sim 24,000 \times 10^3$ Pa/day are the determined best fit parameters, $\tau_0 = 100 \times 10^3$ Pa is an arbitrary reference for dimensional consistency, $T_1 = -1$ °C and $m = 1.92$ are constants, $C = 0.012$ °C^{-1} corresponds to the temperature dependence of Young's modulus, and $sign(\tau)$ is used to preserve the sign, which is independent of n ($n = 3$ for the current set of parameters). Contrary to all the other spatially independent parameters, B is known to include spatially dependent effects that are potentially due to the boundary conditions and crack patterns (Petrich et al., 2015). Extensive modeling and a literature review by Petrich et al. (2015) indicated that B decreased toward the center of a small, 30-m-wide reservoir (from 24,000 to 340 kPa/day), while B was significantly smaller (27 kPa/day) for an essentially laterally unconstrained setting. We adopt the 340 kPa/day value in our analysis and performed sensitivity tests with lower and higher values.

The outstanding feature of the latter relation (equation (13)) is that the model parameters were calibrated against ~1.5 months of in situ thermal stress measurements from the 20- to 70-cm depth range. Registered pressures ranged from +100 to −200 kPa. However, the ability to log tension was limited due to set-up issues (Petrich et al., 2015). Nevertheless, this is dramatically different from all previous studies, which have never been validated with in situ measurements (Attree et al., 2017; Mellon, 1997; Sanderson, 1978).

The above first-order nonlinear ordinary differential equations (equations (12) and (13)) are numerically solved for $\dot{\sigma}$ by using Matlab's ODE45 solver with a 1-s time step and 1-cm grid. The model behaviors under a simple periodic sine variation of the temperature are shown in Appendix D to illustrate the corresponding behaviors and to give an intuitive understanding of the differences between the three presented rheologies.

3.4. Other General Considerations

The tensile and compressive stresses could be symmetric for an ideal periodic variation of the surface temperature around some constant mean temperature, whereas the corresponding ice properties would not exhibit such a symmetry. In particular, the ice strength is smaller in tension and larger in compression (Petrovic, 2003). Ice cracking is therefore more likely to occur in tension, as is the case in many other geomaterials (e.g., Browning et al., 2016). Accordingly, the tensile stress of ice is the main focus of this study.

The tension-compression relationship in the debris mantle could be the opposite to that in ice due to its granular nature and the high fracture strength of rock. It is expected that volumetric contraction of the debris mantle does not lead to fracturing since it can be accommodated by the spatial separation of individual debris particles. However, volumetric expansion may be spatially limited by the collective expansion of particles and therefore lead to the buildup of stresses at locked contacts that may break coseismically when some critical stress can no longer be opposed by friction. Such hypothesis stems from the observations showing minor pulses of seismicity during the local afternoon, most pronounced at the station C1 with the thickest debris mantle (Podolskiy et al., 2018b). To our knowledge, indirect evidence of such behavior has already been investigated in granular materials. For instance, Jia et al. (2009) experimentally investigated the rearrangement of glass beads by thermal cycling through an analysis of sound waves that regularly probed the media. They found that the most significant changes in the granular contact network took place during temperature changes, particularly during the heating phase.

The model output will be compared with a proxy for seismic activity, which is the continuous power spectral density of the relative displacements integrated over the 10- to 30-Hz frequency range (after Podolskiy et al., 2018b). For a visual comparison of stresses with the seismic noise, we show an average depth-integrated stress, $\hat{\tau}$, within the upper centimeters of the layer under consideration, defined as

$$\hat{\tau}(t) \equiv \frac{\int_d^{d+l} \tau_{+/-}(t,z) \quad \mathrm{d}z}{l}, \tag{14}$$

where d is the starting depth of integration (i.e., $d = 0$ corresponds to integration either from the debris surface or from the exposed ice surface), l is the layer thickness, and $\tau_{+/-}$ is either positive or negative stress at a particular time step and depth. Against the background detailed above, we integrate only tensile stresses for the ice ($\tau_+ > 0$ kPa) and only compressive stresses ($\tau_- < 0$ kPa) for the debris mantle. For an overall consistency, instead of a full-depth integration interval, we set l to 10 cm. There are three reasons for such choice: (i) the highest thermal stresses are expected near the surface, where the thermal wave has not been attenuated yet; (ii) we need to separate the type of stresses for ice and debris; and (iii) there is a difference in debris layer thickness among sites. Also, when τ_+ exceeds +100 kPa in the ice (i.e., the lower critical stress threshold according to Colgan et al., 2016), we shade it in red color to assist the eye. It should be noted that the critical stress threshold varies greatly in the literature (from 30 to 400 kPa) and is known to decrease with

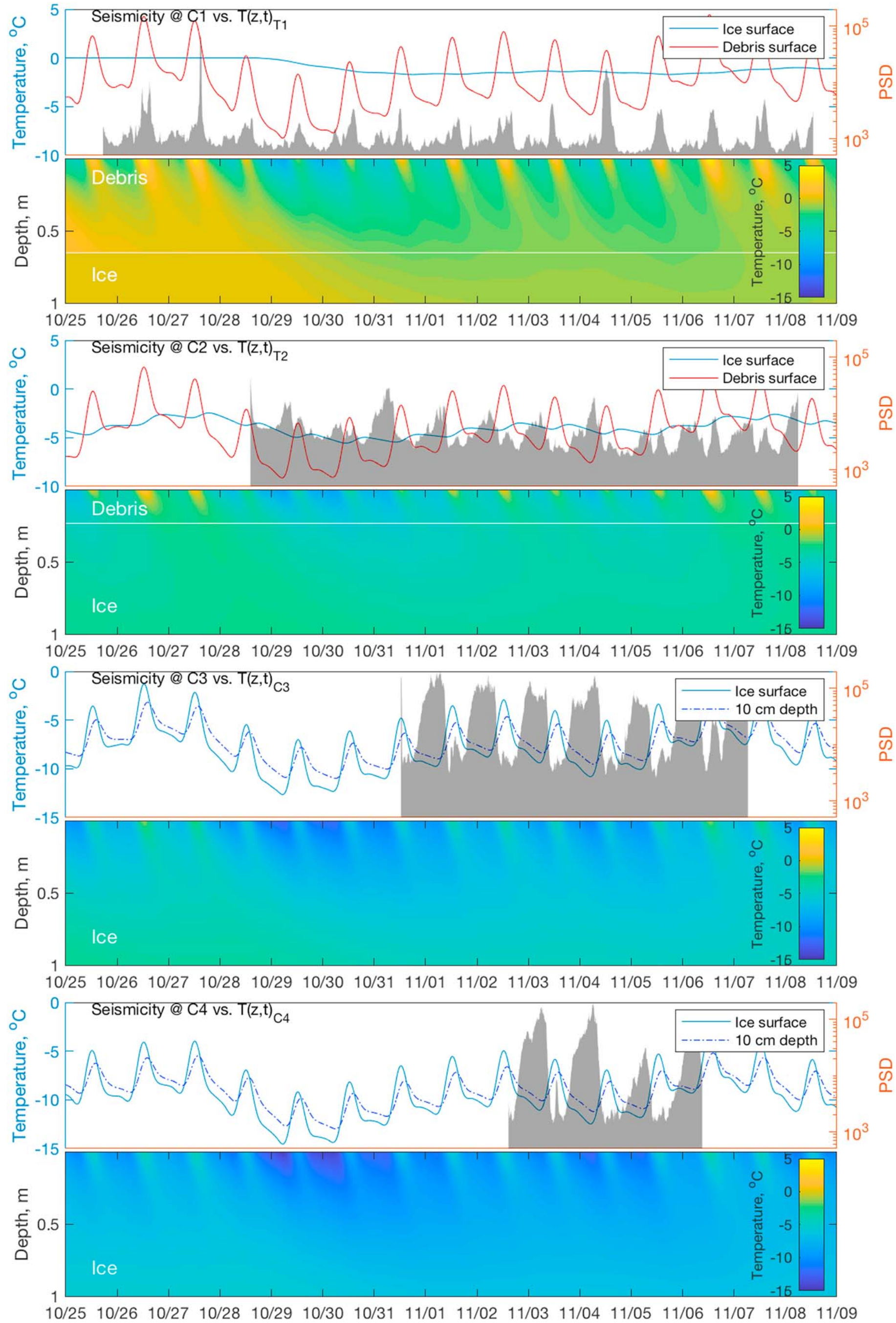

Figure 5. Modeled temperature profiles compared with the observed seismicity, expressed as noise power, at the four sites. The red and blue curves for the debris-covered sites (C1 and C2) represent the temperatures at the debris and ice surfaces, respectively. The blue curves for the debris-free sites (C3 and C4) represent the temperatures at the ice surface and at a depth of 10 cm. PSD = power spectral density.

a higher ice temperature (Colgan et al., 2016) and to increase with a denser crevasse spacing (van der Veen, 1998). Due to the latter facts and the difficulty of a direct comparison between the seismic noise (which varies by orders of magnitude and does not go to zero) and the tensile stress (which can be zero for hours), at this stage we do not attempt to make any quantitative assessments or to establish a link between the critical stress and the noise. Finally, we use local Nepal time (UTC +5:45) throughout the discussion and plots for consistency.

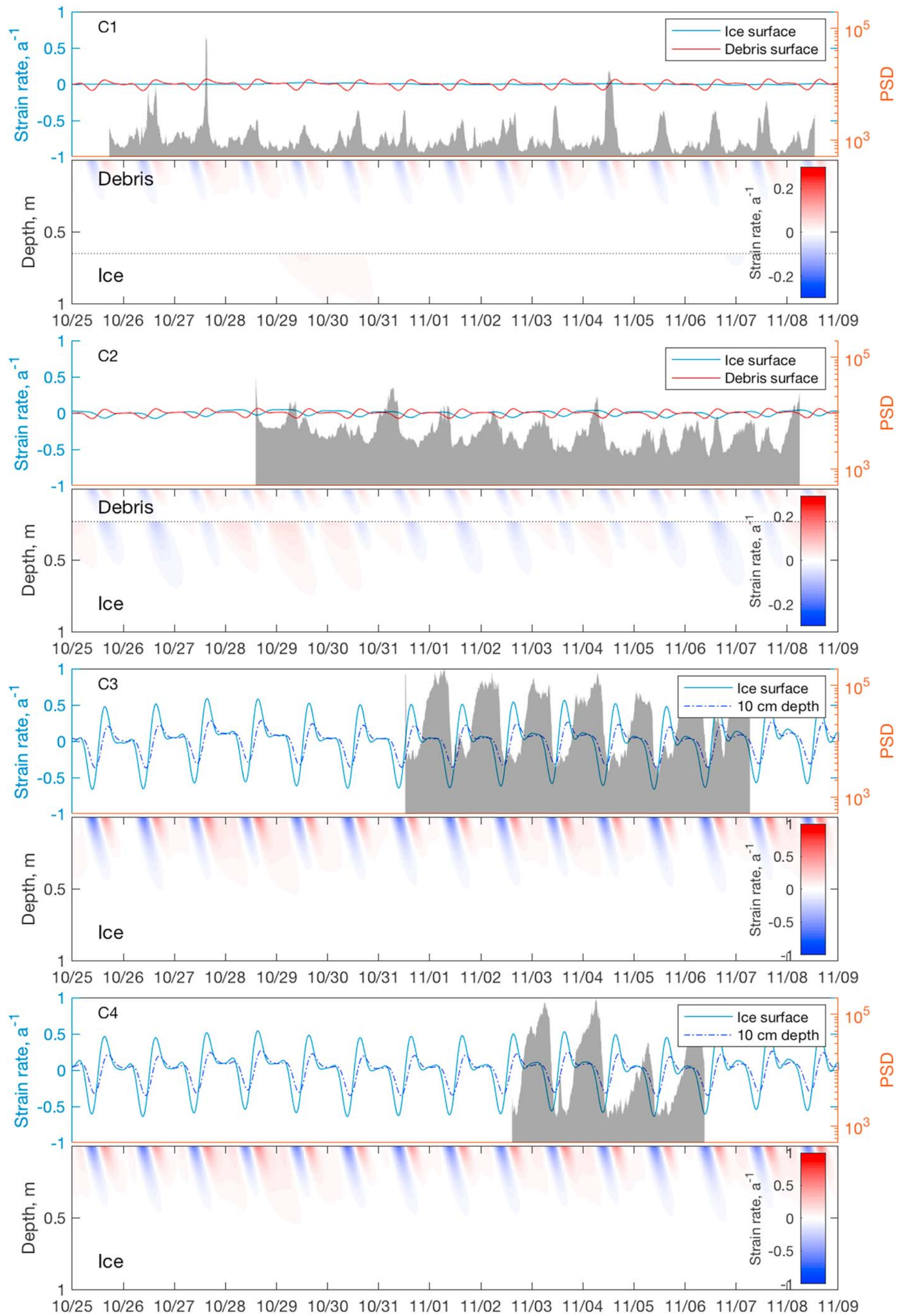

Figure 6. Modeled thermal strain rate profiles compared with the observed seismicity, expressed as noise power, at the four sites. The red and blue curves for the debris-covered sites (C1 and C2) represent the strain rates at the debris and ice surfaces, respectively. The blue curves for the debris-free sites (C3 and C4) represent the strain rates at the ice surface and at a depth of 10 cm. Note that the strain rate colormap limits are different between C1-C2 and C3-C4. PSD = power spectral density.

4. Results and Discussion

4.1. Thermal Profiles and Strain Rates

Figure 5 shows the modeled output for thermal wave propagation in the upper 1 m of the glacier at each site (animated results are provided in supporting information Videos S1–S4). The lower half of the column was relatively warm due to warmer air temperatures in the week prior to the period of interest. The temperature profiles gradually cooled as the autumn season progressed. It was also observed that the temperatures gradually decreased as the site altitude increased from C1 (lowest) to C4 (highest).

It is obvious that the daily temperature cycle is completely attenuated within the upper ~70 cm of the material for each case. The debris mantle at C1 is about 65 cm thick, which means that it effectively shields the ice from the surface air temperature. The thermal wave reaches the ice surface after a lag of ~12 hr. The maximum air surface temperature therefore coincides with the minimum temperature of the buried ice surface. The debris mantle is significantly thinner (~23 cm) and less conductive at C2, such that an attenuated daily temperature cycle penetrates the debris layer and reaches the buried ice surface after a lag of 4–7 hr. The debris-free areas at C3 and C4 experience the highest temperature oscillations due to the lack of a protective debris mantle. The only exception was an observed snowfall event on the evening of 4 November 2017, which may have provided a thin (centimeter-scale) thermoinsulating blanket for the ice (corresponding to the delayed onset in the seismic records discussed below, especially at C4).

Figure 6 presents the corresponding time series of the thermal strain rate variations with depth (Videos S1–S4). The strain rates in ice can be significant, even after attenuation of the thermal wave, due to the marked difference between the expansion coefficients of rock and ice.

The thermal strain rates that reach the buried ice at C1 are barely visible, since they do not exceed 0.02 a^{-1} and therefore do not correspond to an abrupt volumetric contraction. However, the thinner debris mantle at C2 allows for higher thermal tensile strain rates of up to 0.05 a^{-1}. Finally, the maximum thermal tensile strain rates of ~0.6 a^{-1} are modeled for the exposed ice (Figure 6). We used conservative temperatures measured at T2 that were then adjusted for the temperature lapse rate to infer the temperature profiles at C3 and C4 (see Appendix A), such that the exposed ice strain rates can be taken as minimum estimates for C3 and C4. However, these rates are already two orders of magnitude higher than the typical gross strain rates of the glacier (Appendix C).

The critical strain rate criterion has traditionally been associated with crevasse formation, whereas, the critical stress has recently been seen as a more robust criterion (Colgan et al., 2016) and has been used in damage mechanics approach (Girard et al., 2011; Krug et al., 2014; Pralong & Funk, 2005). However, both thresholds can be imprecise because the local mechanical properties of the ice are crucial (especially ice fracture toughness; Colgan et al., 2016). According to the review by Colgan et al. (2016), the critical strain rate threshold for crevasse formation is 0.02–1.1 a^{-1} for glacier ice with a mean annual temperature of approximately −10 °C. It is therefore observed that the minimal reported strain rate thresholds for crevasse formation are easily reached at almost all the sites, including the debris-covered ones, due to the high diurnal temperature amplitude along the glacier.

The following features are observed from a comparison of the energy and temporal fluctuations of the seismic noise (Figure 5): (i) the seismicity and noise levels are the weakest at the site with the thickest debris mantle (C1); (ii) the noise is about an order of magnitude higher at the site with the thinner debris mantle (C2); and (iii) is almost 2 orders of magnitude higher at the debris-free areas around C3 and C4. Furthermore, a weak but sharp noise peak occurs at noon at C1, whereas the main noise peaks at C2–C4 occur after midnight or early in the morning.

It could be argued that the weak afternoon peak at C1 corresponds to a moment when a delayed thermal contraction wave penetrates the buried ice beneath a thick debris mantle. However, since the temperature drop is insignificant at the buried ice surface, rather than being sharp, and does not lead to strain on a daily basis, we believe that such an interpretation is highly unlikely. We therefore suggest that alternative mechanisms are more reasonable, such as thermal-expansion-induced rearrangements of the debris particles (section 3.4) or wind (although the latter was weak and less correlated with seismicity; Podolskiy et al., 2018b). For example, a covariance of the noise power with the compression of the upper ~10 cm of the debris cover can be seen in Figure 7a.

The night peak in seismicity at C2 occurs after the minimum air surface temperature and before the lowest temperature at the buried ice surface. The seismic peaks at C3 and C4 exhibit almost no lag relative to the surface temperature, confirming the general idea that debris attenuates and delays the thermal contraction wave.

The thinner debris mantle at C2 is the most sensitive to our choice of debris properties during the modeling. In particular, decreasing the debris thickness by 10 cm, or halving the thermal conductivity or density does not assist in propagating the diurnal temperature fluctuation to the buried ice surface at C1; whereas the same debris property variations at C2 are equally sufficient in producing higher stresses and a better match

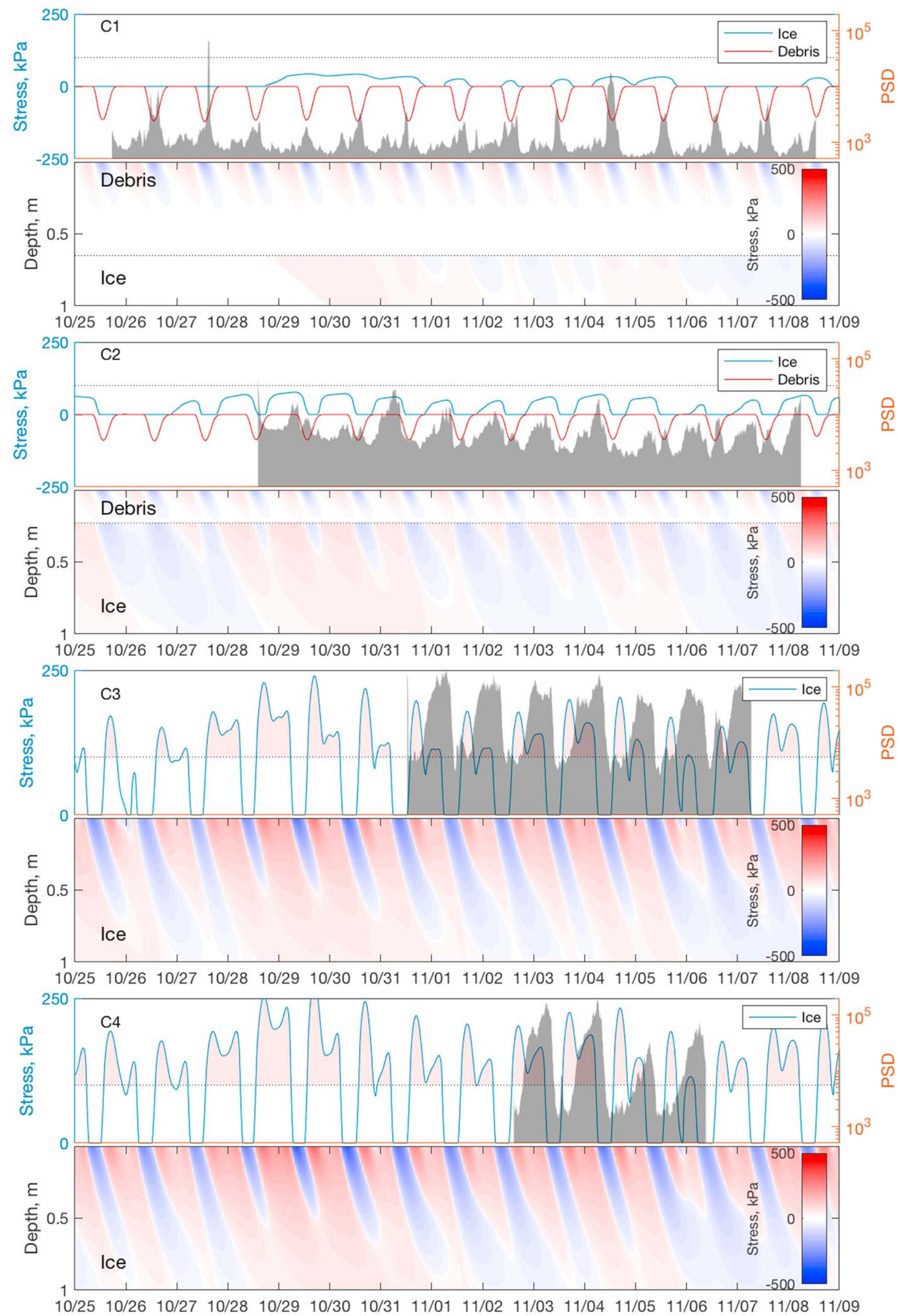

Figure 7. Modeled stress profiles (elastic for debris and viscous for ice; after Sanderson, 1978; equation (10)) compared with the observed seismicity, expressed as noise power, at the four sites. The red and blue curves for the debris-covered sites (C1 and C2) represent the average depth-integrated stresses, $\hat{\tau}$, near the debris and ice surfaces, respectively. The blue curves for the debris-free sites (C3 and C4) represent $\hat{\tau}$ near the ice surface; the stresses are shaded in red when they exceed the lower critical stress threshold, shown by the dotted line (Colgan et al., 2016).
PSD = power spectral density.

between the timing of the thermal wave reaching the ice surface and the observed seismicity. Given that C2 is in an area where the debris continues to thin, becomes spatially discontinuous, and completely disappears ~700–800 m upglacier, it is reasonable to expect a gradual loss of this debris-insulating effect, which leads to convoluted features of the areal seismic response and therefore makes it difficult to separate macroscale and mesoscale spatial effects. This aspect cascades through all our results and the discussion related to C2.

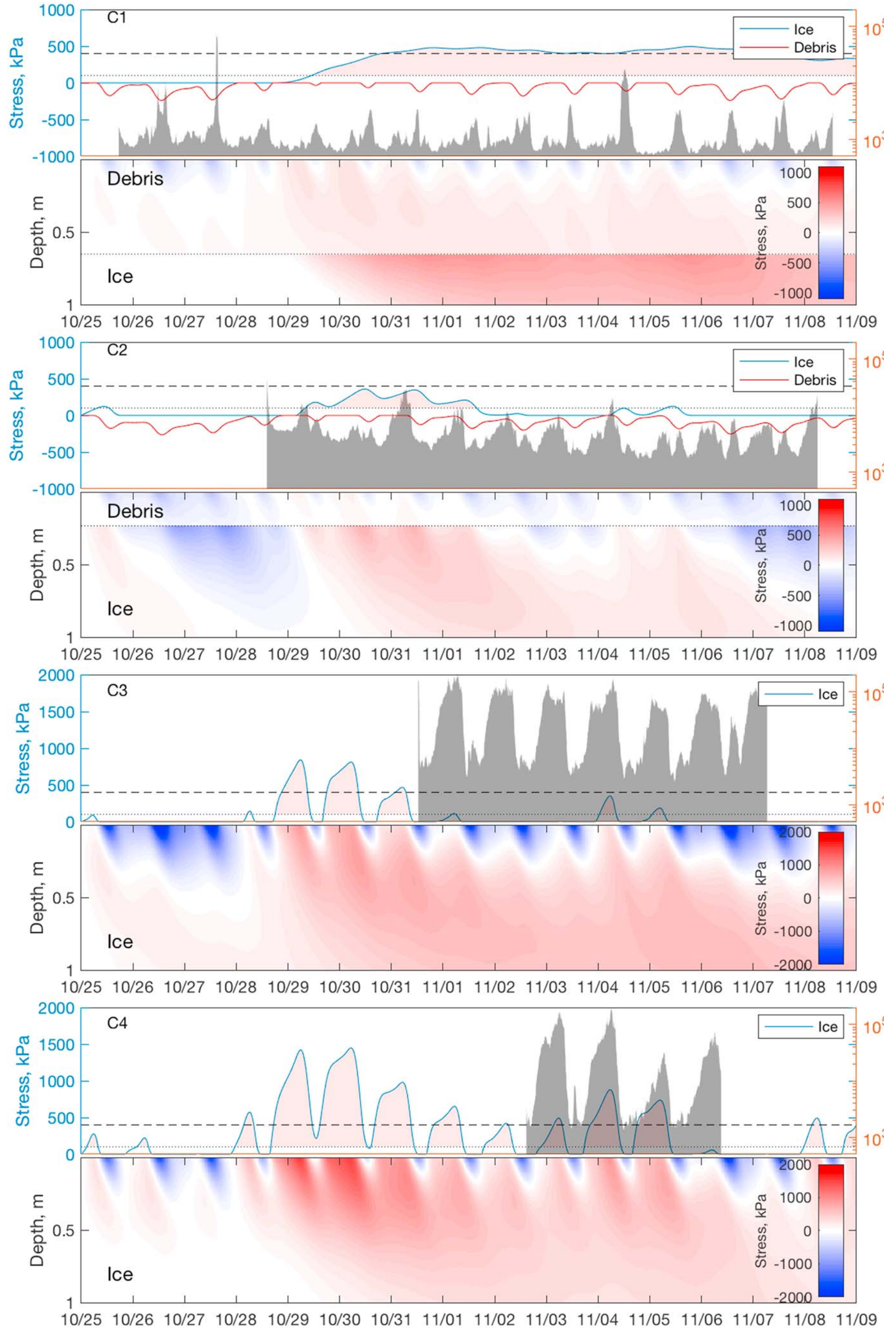

Figure 8. Unfiltered modeled stress profiles (elastic for debris and elastic for ice; according to equation (11)) compared with the observed seismicity, expressed as noise power, at the four sites. The red and blue curves for the debris-covered sites (C1 and C2) represent the average depth-integrated stresses, $\hat{\tau}$, near the debris and ice surfaces, respectively. The blue curves for the debris-free sites (C3 and C4) represent $\hat{\tau}$ near the ice surface. The stresses are shaded in red when they exceed the lower critical stress threshold, shown by the dotted line; the dashed line shows the upper critical stress threshold (Colgan et al., 2016). Note that the stress scales and colormap limits are different between C1-C2 and C3-C4. PSD = power spectral density.

10.1029/2018JF004848

Nevertheless, these results largely explain why the debris-covered area around C2 experiences a nocturnal increase in seismicity similar to that at C3 and C4, but with noise maps (referred to as Power Spectral Density-Probability Density Functions (PSD-PDFs) by Podolskiy et al., 2018b) that resemble those at C1. For example, the observed icequakes near C2 have smaller amplitudes than those at C3 and C4 due to the attenuated temperature fluctuations.

Furthermore, we note that minor secondary peaks of amplified noise occur during the afternoon at C2–C4 as the surface temperature drops. These small peaks appear to increase after a snowfall event on 4 November, especially at C2 on days with surface temperature close to zero in the afternoon (Figure 5). These conditions could lead to the melt of a new-fallen snow and to more meltwater production at the surface. We speculate that the most plausible explanation of the secondary peaks is the rapid refreezing of a meltwater film near the surface that leads to a volumetric expansion within small ice cracks or flaws between the debris particles. Meltwater-induced fracture seems a less likely interpretation, given the insignificant amount of melt.

4.2. Thermoviscous Stress

Colgan et al. (2016) suggested that the critical stress threshold for crevasse formation was 100–400 kPa for glacier ice with a mean annual temperature of approximately −10 °C, whereas the threshold may be only 100–200 kPa for warmer ice (−5 to 0 °C). The stresses computed using the purely viscous model (Figure 7) reached the critical stress values at the exposed ice sites and came close to them at C2 (80 kPa). Furthermore, the tensile stress can exceed 200 kPa in the upper 5 cm of ice and reach 50 kPa at 50 cm depth at the exposed ice sites (C3 and C4).

However, the timing of the highest thermal tensile strain rates does not coincide with the most intense seismicity observed at the exposed ice surfaces (Figure 6), which means that neither the strain rate criterion nor a purely viscous stress model (that is a function of a thermal strain rate, equation (10); Figure 7) can be adopted as satisfactory interpretations of our observations.

The increase in seismicity should occur 4–5 hr earlier if the rate of surface cooling is the only driver of the cracking front propagating ~60 cm below the ice surface, with the upper 15 cm of ice experiencing the highest rate of volumetric change. However, cross-correlation (Podolskiy et al., 2018b) and simple visual inspection of the modeled temperature profiles at the debris-free sites suggest that the night "explosion" in seismicity occurs when ice "feels" the coldest diurnal temperature (Figure 5). One could argue that such a delay corresponds to the time required for the tensile stress wave to propagate a certain depth below the ice surface, with this wave capable of generating new cracks and keeping the near-surface seismically active until the stresses are attenuated. The 20- to 40-cm depth range should correspond to the start and abrupt end of seismicity observed at C3 and C4. However, inspection of the corresponding stresses at these depths suggests that the viscous stresses show a rapid drop below 100 kPa.

We therefore suggest that a purely viscous model of ice is not sufficient to generate realistic results, which indicates that an elastic or viscoelastic models needs to be employed.

4.3. Thermoelastic Stress

Results of the purely elastic model are presented in Figure 8. They correspond to extremely high amplitudes of stress, for example, +1500 kPa exceeds the tensile strength of ice, despite the low value of the assumed Young's modulus (Appendix D). Here, we note that the real temperature variation is not symmetric and has a trend or long-period oscillations (i.e., days) that may cause a gradual drift in static stress from the initial condition. We therefore apply a high-pass filter to the result to avoid such long-term drift (i.e., only allowing fluctuations with a period shorter than 48 hr), since our primary focus is on the diurnal cycle (this also applies to debris stresses in all other figures except Figure 8).

The filtered elastic model may produce stresses of up to 50 kPa at 50-cm depth, as shown in Figure 9. However, the stress magnitudes close to the ice surface, as well as their timing, are dramatically different from the viscous results. The viscous tensile stress does not exceed ~250 kPa and reaches its maximum early in the evening, whereas the elastic tensile stress is as high as 650 kPa and peaks late at night. The timing and temporal variation of the elastic stress amplitude agree reasonably well with the observed seismic activity (Figure 9).

Here we have computed the purely elastic stress by simply filtering out the long-term stress accumulation. Incorporation of the viscosity should correspond to a similar effect, the long-term stress relaxation.

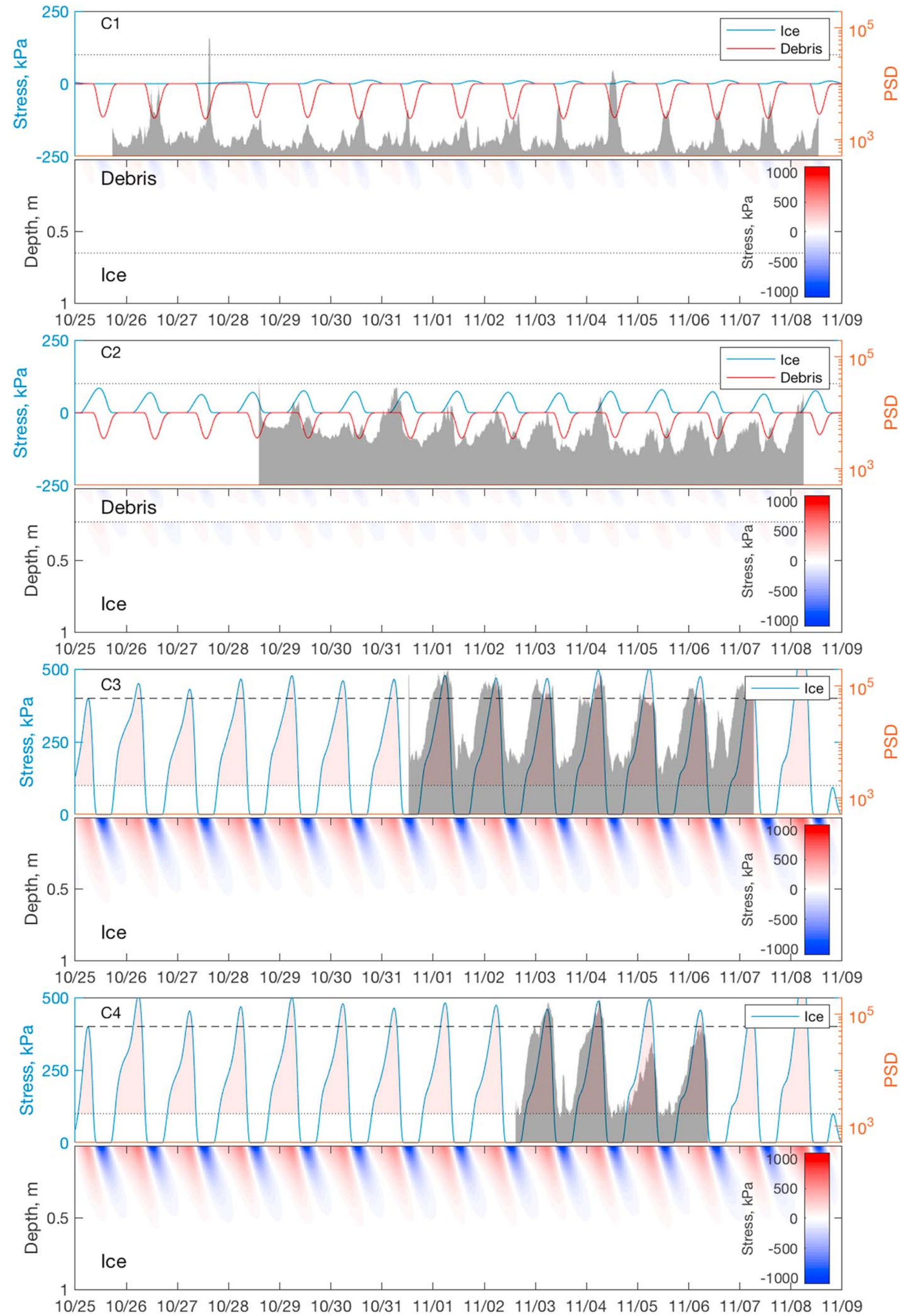

Figure 9. Filtered modeled stress profiles (elastic for debris and elastic for ice; according to equation (11)) compared with the observed seismicity, expressed as noise power, at the four sites. The red and blue curves for the debris-covered sites (C1 and C2) represent the average depth-integrated stresses, $\hat{\tau}$, near the debris and ice surfaces, respectively. The blue curves for the debris-free sites (C3 and C4) represent $\hat{\tau}$ near the ice surface. The stresses are shaded in red when they exceed the lower critical stress threshold, shown by the dotted line; the dashed line shows the upper critical stress threshold (Colgan et al., 2016). Note that the stress scales are different between C1-C2 and C3-C4. PSD = power spectral density.

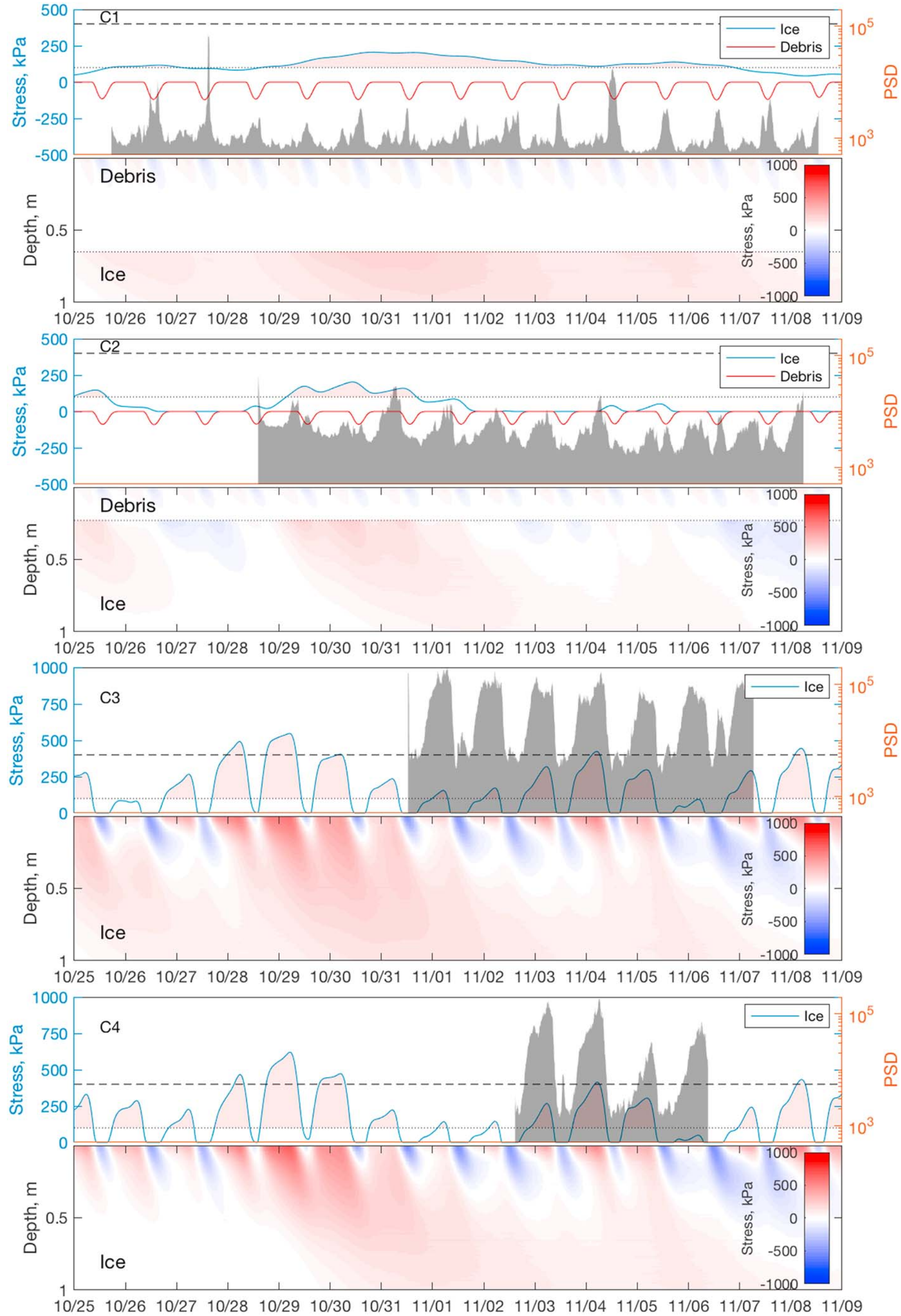

Figure 10. Modeled stress profiles (elastic for debris and viscoelastic for ice; after Petrich et al., 2015; equation (13)) compared with the observed seismicity, expressed as noise power, at the four sites. The red and blue curves for the debris-covered sites (C1 and C2) represent the average depth-integrated stresses, $\hat{\tau}$, near the debris and ice surfaces, respectively. The blue curves for the debris-free sites (C3 and C4) represent $\hat{\tau}$ near the ice surface. The stresses are shaded in red when they exceed the lower critical stress threshold, shown by the dotted line; the dashed line shows the upper critical stress threshold (Colgan et al., 2016). Note that the stress scales are different between C1-C2 and C3-C4. PSD = power spectral density.

4.4. Thermoviscoelastic Stress

The above tests strongly suggest that the purely viscous behaviour of ice is insufficient to explain the results, whereas an elastic behaviour is necessary. These lines of evidence indicate that viscoelastic rheology is needed for dealing with thermal stresses in ice.

Our ice rheology models in Appendix D demonstrate that a selection of parameters for the Maxwellian thermoviscoelastic model with the classic Glen-Nye rheology is not a straightforward task, since the conventionally chosen parameters cannot be readily adapted to the near-surface ice and require unrealistically cold temperatures to activate the elastic response. We therefore find that the only readily applicable approach, that does not require extensive tuning, is the calibrated model of Petrich et al. (2015), which we employed to calculate the stresses shown in Figure 10.

As expected, the corresponding viscoelastic results mimic the purely elastic and purely viscous tests, with the diurnal temperature leading to a significant tensile stress peak after midnight in the upper 10 cm of the ice, which is more pronounced during cold spells (e.g., 28–30 October 2017). The stress relaxation due to creep leads to smaller diurnal stress oscillations than those estimated by the purely elastic model. The ice profiles remain under slight tension or compression due to a hysteresis from the temperature trend of the preceding few days and the ability of creep to relax these accumulated stresses (faster at low altitudes and slower at high altitudes; Figure 10).

The alternating timing of the largest tensile and compressive stresses at the exposed-ice sites agrees reasonably well with the peaks in seismic activity. In particular, the seismicity quickly ceases as the ice surface enters a compressive mode and restarts less abruptly when the compression wave is still dissipating through the upper ∼25 cm of the ice (and therefore arresting the opening of cracks). We also observe that while purely elastic or purely viscous models yield tensile stresses of ∼50 kPa at 50-cm depth, the viscoelastic model produces unrelaxed stresses that can exceed 150 kPa and last for days, at similar depths. This suggests that the background stress could enable fracturing at cold surface temperatures, even in the daytime, and that this intensifies at night.

We find that the calibrated Maxwellian viscoelastic approach performs well, but it cannot be further improved in a realistic sense without in situ thermal stress measurements near the glacier surface, which, to our knowledge, have not been acquired to date. Furthermore, it is important to realize that the best-fit calibration does not have a single solution and always corresponds to a vast parameter space (e.g., with an n value that spans the 3.0–4.5 range, and A in the 131- to 200-kPa/°C range; Petrich et al., 2015), even though it is constrained by observations.

Finally, we note that the temporal pattern of the presented elastic and viscoelastic tensile stresses corresponds to the highest cumulative thermal tensile strain. In other words, the seismicity intensifies as the strain switches from compression to tension, and ceases as the strain field switches back to compression (Figure 11). This suggests that the near-surface cracks will first open, which then leads to the observed seismicity.

4.5. Sensitivity Tests

We performed sensitivity tests using a higher specific heat capacity for the debris mantle (948 $J \cdot kg^{-1} \cdot K^{-1}$; Reid & Brock, 2010). This higher specific heat capacity (i.e., a lower thermal diffusivity of the debris mantle) leads to a faster attenuation of the diurnal temperature fluctuation signal, and therefore a slightly shallower penetration of the diurnal thermal disturbance.

The sensitivity of the estimated thermoviscoelastic stress to B in equation (13), which is considered a spatially varying parameter (Petrich et al., 2015), is illustrated in Figure 12. The stresses at the surface correspond to the T2 temperature records and the assumption of no debris mantle. A smaller B value (e.g., 27 kPa/day) yields a more elastic response, and vice versa. A higher B value indicates a more viscous behaviour that shifts the stress signal (and its peak) to earlier timing and reduces its amplitude. An increase in B can therefore lead to enhanced creep in softer or warmer ice, which does not apply to our conditions.

We then fixed B at 340 kPa/day to investigate the stress sensitivity to different debris mantle thicknesses and physical properties, as shown in Figures 12b and 12c. A 40- to 60-cm-thick debris mantle is sufficient to filter out the diurnal stress fluctuation (the range is due to a sensitivity to the thermal conductivity of the debris mantle).

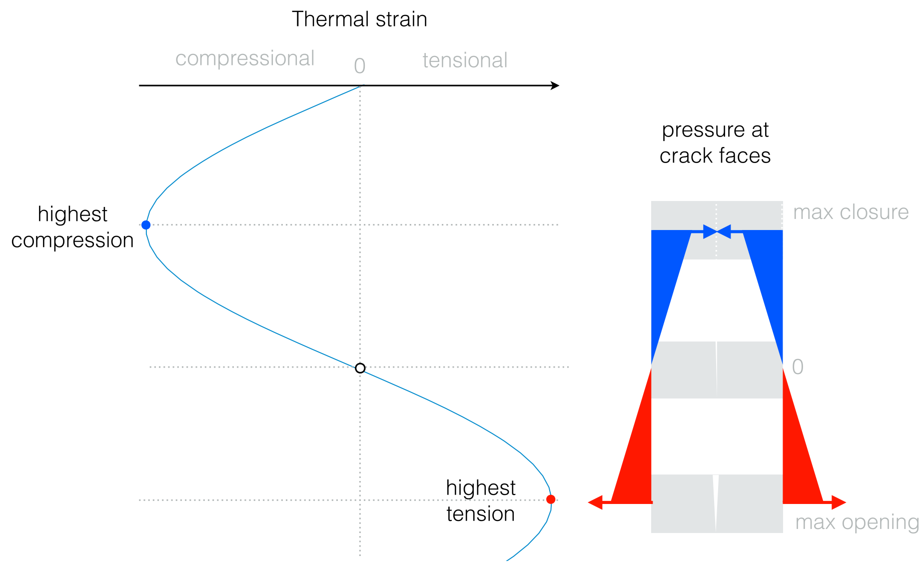

Figure 11. Schematic representation of the relationship between the overall thermal strain and pressure conditions at an individual ice crack. The compressional thermal strain (i.e., at the warmest temperature) arrests crack propagation, whereas the tensional strain (i.e., at the coldest temperature) favors crack propagation. The thermal strain should first sufficiently open preexisting cracks prior to the occurrence of any icequakes.

However, it is important to note that the earlier cited example of reported thermal cracks in ice beneath a 0.38- to 0.7-m-thick debris mantle in Antarctica's Dry Valleys (Marchant et al., 2002) is still in agreement with our modeling framework. We therefore conducted a test to mimic these Antarctic parameters by reducing the mean annual temperature to −34 °C and employing debris properties similar to those measured near C1. Our model results (using B values of 27 and 340 kPa/day) demonstrate that the critical stress threshold of 100 kPa (Colgan et al., 2016) can be exceeded for days despite a 70-cm-thick debris mantle, especially for a lower B value (Figure 12d).

Our analysis of the aforementioned uncertainty in the rheological parameters of the near-surface ice (e.g., the B value), stress dependence on the debris properties (e.g., the thermal conductivity, density, and specific heat capacity), and adaption of strength theory as a basis for this study all indicate that the search for a site-specific critical stress threshold for crack initiation remains challenging.

4.6. Weathering Crust Ice

Our analysis suggests that the large diurnal amplitude in air temperature, with its rapid cooling trend, which is typical for the Trakarding-Trambau Glacier system, could be a crucial parameter that controls the intense contraction-induced fracturing at night. However, the importance of this feature is still unclear. For example, Sanderson (1978) reported a daily amplitude of ~5 °C in coastal Antarctica (but omitted this from his thermal stress analysis), and the snowquakes reported by Nishio (1983) in continental Antarctica occurred in a region where the daily amplitude was about 6.25 °C. Since our case of intense ice fracturing during cooling is rare outside the polar regions, it may indicate that site-specific characteristics need to be identified and addressed in future studies. If defects and inherent weakness are important causes of fracturing, then why are they more pronounced in the ablation area of the considered glacier system compared to other glacial regions, like Greenland or Alps? This question becomes even more important if the large diurnal temperature fluctuations are not a unique or sufficient feature to explain the observation.

Previous observational and experimental studies on contraction-induced fracturing in rock (Browning et al., 2016) and snow (Nishio, 1983) noted that one of the fracture characteristics is an isotropic (or random) occurrence. This suggests that as we search for reasons of inherent weakness, we should look for some nonlocalized phenomenon or process.

An alternative possibility is that the upper layer of ice may correspond to a so-called “weathering crust,” which consists of supraglacial porous ice that develops seasonally over an ablating glacier surface (Cook et al., 2016; Hoffman et al., 2014). An overview of the limited literature on weathering crust ice by

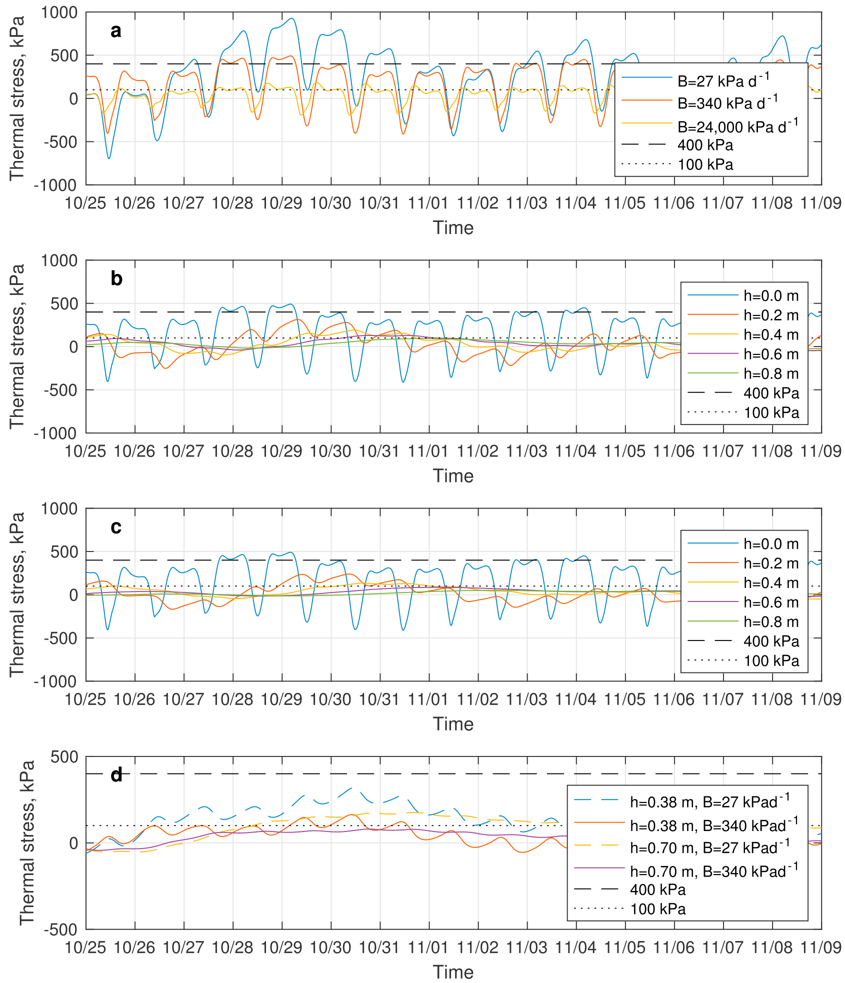

Figure 12. (a) Sensitivity of the computed thermoviscoelastic stress to B value (equation (13)). Note how the timing of the nocturnal peak shifts from "after midnight" to "before midnight" as the B value increases (i.e., viscous behavior dominates). The air temperature corresponds to T2, and a debris mantle thickness of 0 cm is assumed. (b, c) Attenuation and stress delay (for the T2 air temperature measurements and B = 340 kPa/day) for a debris mantle of varying thickness and the debris physical properties measured near C1 (b) and C2 (c). (d) Synthetic test with an artificially reduced mean air temperature ("T2(t)"−33.43 °C) and a debris mantle thickness of 0.38 or 0.7 m for a simplified comparison with the conditions observed by Marchant et al. (2002). The dashed and dotted lines show the critical stress range (Colgan et al., 2016).

Cook et al. (2016), suggested that the maximum rates of weathering crust evolution were connected to clear sky conditions, when incoming shortwave radiation dominated the surface energy balance. Rapid evolution of weathering crust means a progressive increase in overall ice porosity due to subsurface melt, which enlarges the interstitial spaces and disaggregates crystals, and therefore enhances heat flow. Development of such "rotten" or "honeycomb" ice translates to low-density (e.g., 400 kg/m^3) surface ice that undergoes a nonlinear increase to 900 kg/m^3 in the upper tens of centimeters (Cook et al., 2016; Cooper et al., 2018). Hoffman et al. (2014) reported a low density in the upper 10–20 cm of glaciers in the Dry Valleys, Antarctica, and estimated that the upper few centimeters of the surface consisted of crumbly ice with a density between 400 and 750 kg/m^3. Cooper et al. (2018) found that the ice density was affected by ablation down to 1.1-m depth, with a weathering crust density of 330–560 kg/m^3 in the western Greenland Ice Sheet ablation zone. To our knowledge, no rheological tests on weathering crust ice or analyses of regional differences are available in the literature.

The high shortwave incident radiation at the Trakarding-Trambau Glacier system, with a mean value of 228.2 W/m^2 and an average daily peak of 958 W/m^2 during the campaign, in combination with the number of small mineral particles that penetrate the ice surface due to strong solar heating, suggest that the necessary environmental conditions are present across the Trakarding-Trambau Glacier system for the rapid development of a weathering crust. Such a crust should be associated with many microvoids, leading to a weaker effective strength and lower stiffness than that of pure ice. However, it is also logical to suggest that the debris-covered areas are unlikely to have a well-developed weathering crust, as the debris mantle would block solar radiation, thereby preserving a competent ice surface beneath the debris mantle (i.e., higher critical stress threshold). The current belief is that internal near-surface melt due to solar radiation drives weathering (Hoffman et al., 2014). However, taking into account our numerical experiments and previous reports on thermal cracks under a debris mantle (Marchant et al., 2002), we argue that nocturnal thermal contraction cracking can also contribute to mechanical damage to near-surface ice since it can penetrate a thin debris mantle. Moreover, we speculate that such thermal cracking may have some positive feedback by enhancing previously generated fractures.

5. Conclusions and Outlook

We used four composite rheological models to simulate the thermal stresses in near-surface ice with or without an overlying debris mantle to determine the ice rheology that best reproduces the nocturnal ice fracturing observed at the Trakarding-Trambau Glacier system in high-altitude Himalaya by Podolskiy et al. (2018b). The purely elastic model (with a long-term stress accumulation filtered out) and calibrated Maxwellian viscoelastic model explain the observations reasonably well and confirm that the debris mantle modulates the stresses by filtering out the diurnal temperature fluctuations. We also demonstrate that the observations cannot be reproduced when elasticity is omitted from the thermal stress calculations for the near-surface part of the glacier (Sanderson, 1978). Furthermore, the described model can be readily adapted to other case studies since the debris mantle can be numerically modified to represent a snow layer or a regolith (Ferrari, 2018).

Further improvements can be made to the current models, including the incorporation of radiative heating and cooling, and refreezing (e.g., MacAyeal et al., 2019), the introduction of the Finite Difference scheme (Appendix B) for the heat equation to deal with complex profiles of physical properties (e.g., thermal conductivity), a more sophisticated rheology of granular debris cover, and an extension to the fracture mechanics (e.g., Bazant, 1992). Moreover, alternative viscoelastic constitutive relationships for ice should be tested, for example, material models with finite-viscosity laws may be useful (e.g., Riesen et al., 2010). At this point, it remains unclear whether the amplitude of seismic noise can be used as a proxy for the amplitude of stress, and therefore it is difficult to judge how adequate is the viscous relaxation in the calibrated Maxwellian viscoelastic model. Previous numerical modeling by Petrich et al. (2015) illustrated that determining the optimal viscoelastic parameters to reproduce the measured thermal stresses in reservoir ice is a demanding task due to multiple solutions and site-dependent parameters. We also acknowledge that the search for the "right" parameters for near-surface glacier ice may remain a heavily debated topic unless it is supported by detailed in situ mechanical experiments that elucidate local and regional differences. Detailed seismic waveform modeling further constraining mechanisms associated with thermal fracture may be also helpful for inverting physical properties of ice near the surface.

This study demonstrates that the topic of thermal stress in terrestrial glaciers has received relatively little attention to date and has been overlooked as a potentially important weathering agent. However, it is expected that the seismic signature of such stresses will be observed more frequently due to the increasing number of cryoseismic experiments on Earth and other bodies in the Solar System. Our results suggest that new high-mountain alpine experiments and growing seismic networks in continental Antarctica and Greenland (e.g., Podolskiy & Walter, 2016) should observe intense thermal cracking at sites with a negative mass balance (i.e., no snow layer over glazed surfaces or over blue ice; Nishio, 1983). We therefore believe that the subject of thermal stress warrants further investigation to better understand seismic noise and the weathering of ice bodies.

Appendix: A: Empirical Temperature Model

An eight-term sum-of-sines model (equation (4)) yielded the best fit to the air temperatures measured at each site, which is indicated by the red curves in Figure 2, with an average R^2 and root-mean-square error of 0.88 and 1.2 °C, respectively. However, the construction of this model exposed several issues and the need to make key adjustments, as detailed below.

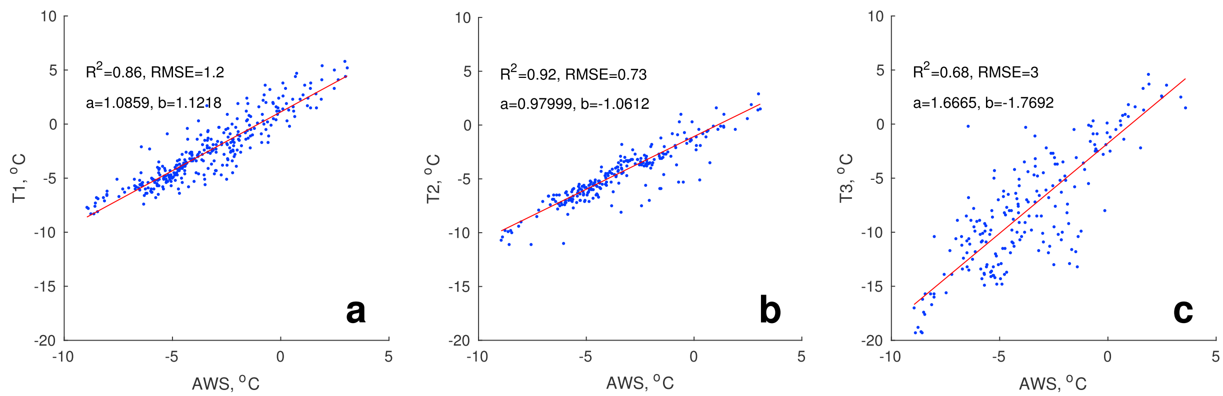

Figure A1. (a–c) Scatter plots of the surface air temperature measured at the AWS and T1–T3, along with their corresponding linear fits, and goodness-of-fit qualities and coefficients. AWS = autonomous weather station; RMSE = root-mean-square error.

First, the only complete time series for the period of interest was at the AWS site. For example, T1 was only back online after noon on 26 October 2017, whereas the data at T3 could only be retrieved up to 2 November 2017.

Second, out attempt to fit the T2 temperature measurements (Figure 2) yielded underestimated amplitudes prior to the maintenance visit on 29 October 2017, and a good fit afterward. Furthermore, if we extend the time period, such that the fit extends one week earlier, the opposite result is obtained (i.e., good fit to the amplitudes prior to the maintenance and overestimated amplitudes afterwards). This suggests that the measurements are only reliable after the sensor reinstallement on 29 October 2017, due to an instrumental issue (e.g., a fallen sensor).

Third, Fourier and other closely related series (sum-of-sines in our case) are known to be unreliable (i.e., diverge rapidly) outside the data set used to obtain the best fit. This is especially relevant here since our initial conditions for the temperature profiles will inherit these features. Low-frequency signals (i.e., periods of days) can lead to artifacts in the background temperatures of the debris and ice. We therefore start our fits one week prior to the first day in our period of interest to avoid the latter concern, and note that studies aiming to obtain temperatures deeper than 1 m below the ice surface need a significantly longer margin. This approach corresponds to a relatively warm temperature profile that gradually cools with time due to the warmer conditions in the week preceding the start of our field campaign.

It appears reasonable to rely on the AWS measurements, and apply these observations to the other locations (T1–T3) by establishing corresponding regression models with each site, which avoids the introduction of low-frequency artifacts and the usage of an incomplete time series. Figure A1 shows the scatter plots for air temperature simultaneously measured at the AWS and each of the other sites (T1–T3). We use only the shared time period after the maintenance visit for the AWS–T2 comparison, based on the above discussion. We observe that the largest disagreement in terms of goodness-of-fit qualities is in the AWS–T3 plot, noting that T3 is the highest and most remote site from the AWS. However, the much larger amplitude variation could be due to the actual sensor height, which could be zero because of a fallen sensor, leading to a high amplitude due to radiative warming and cooling. We therefore run the models with the T2 temperatures (adjusted for the elevation difference using a standard temperature lapse rate of 6.5 °C/km) as an input to avoid the possibility of using biased measurements, along with no debris mantle sites, as a conservative reference for sites C3 and C4.

Table A1
Key Model Inputs for Each of the Seismic Station Locations

Station	T(0,t)	Debris thickness, m
C1	T1	0.65
C2	T2	0.23
C3	T2−(0.511 × 6.5)	0
C4	T2−(0.777 × 6.5)	0

The corresponding linear fits (i.e., slope, a, and offset, b) are used as a simple way to transform the AWS measurements to each individual site (Figure A1). Finally, the sum-of-sines fit is determined for each transformed data set and used as an input boundary condition, $T(0, t)$, for the heat-conductivity equations. The input parameters at each seismic station for the conducted model runs are summarized in Table A1.

Appendix B: FDM for Heat Diffusion

Diffusion equation describing a propagation of heat through a multilayer media can be solved by semi-analytical (Carr & March, 2018) and numerical schemes (Jafarov et al., 2012), including the FDM (Hickson et al., 2011). The convergence of different approaches and description of the interface condition

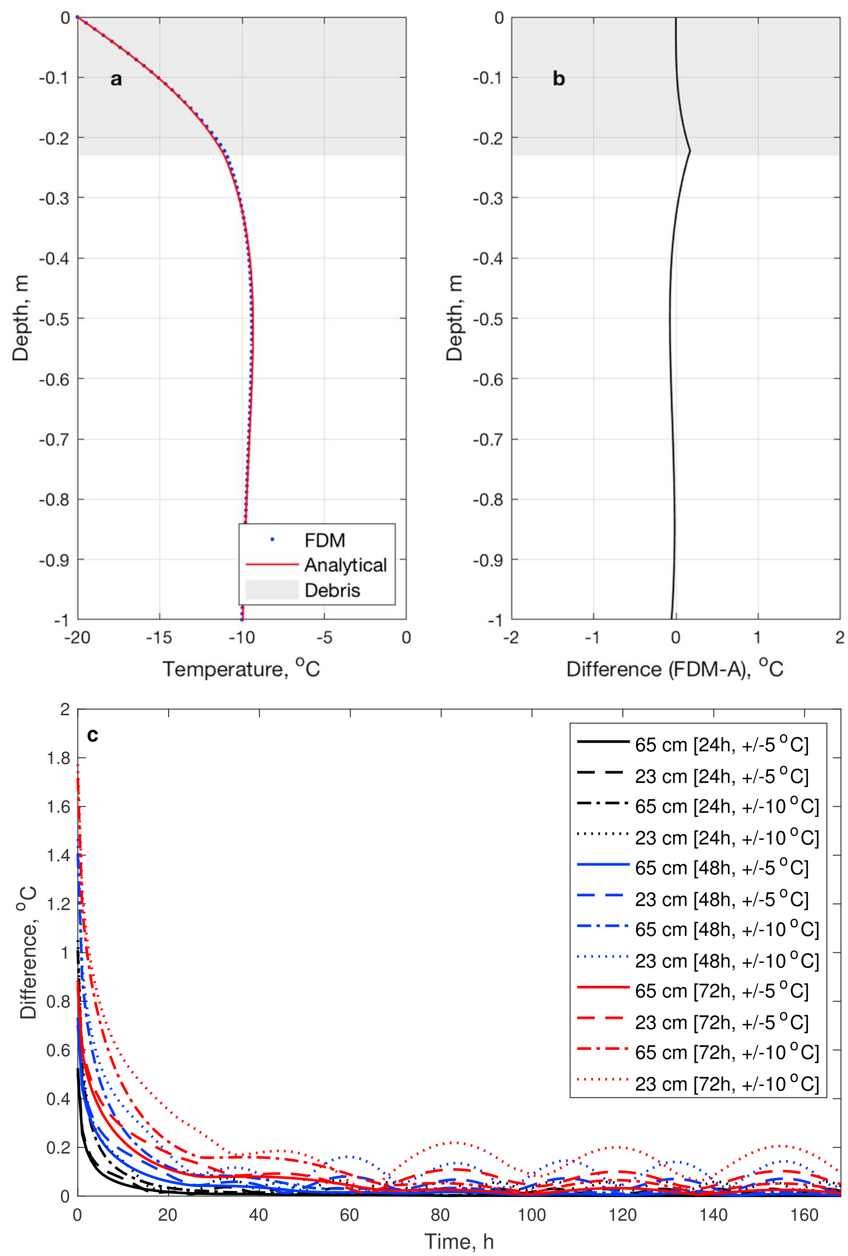

Figure B1. (a–b) Example of the analytical and FDM solutions of the heat-diffusivity equation for a two-layer media, along with their corresponding differences. (c) Convergence of analytical and FDM solutions with time for a variable layer thickness and variable heat wave properties (i.e., higher periods and amplitudes correspond to deeper penetration depths and higher gradients). The shown "difference" is defined as a depth-integrated average absolute difference between the solutions. FDM = Finite Difference Method.

between two layers is a topic of active research without a single universally accepted method for multilayer problems having time-varying boundary conditions (Carr & March, 2018; Hickson et al., 2011). For example, a contact can be "perfect" or have a "jump," or a smoothed version of a piecewise profile can be used. Due to this, a lack of an appropriate temperature profile, and due to a "never-steady" state of the active layer under discussion, a comparison between the simple approach applied in our study (equation (5)) and other methods is not a straightforward task.

Nevertheless, below we use a time-forward and space-central finite difference approximations to make a validation test. Specifically, for a vertically heterogeneous medium with a depth-dependent diffusivity, α, the continuous 1-D heat equation (equation (1)) can be expressed in a discretized form for a spatial grid with Δx space between computational nodes and a time step, Δt:

$$T_i^{n+1} = T_i^n + \frac{\Delta t}{\Delta x^2}\left(0.5(\alpha_{i+1} + \alpha_i) \times (T_{i+1}^n - T_i^n) - 0.5(\alpha_{i-1} + \alpha_i) \times (T_i^n - T_{i-1}^n)\right), \tag{B1}$$

where n and n+1 are the current and the consequent time steps, respectively, and i is the location of the node. For a stable solution, Δt should satisfy the Courant-Freidrich-Lewy condition ($\Delta t \leq 0.5\frac{\Delta x^2}{\max(\alpha)}$). Assuming the same temporal/spatial grids and cosinusoidal surface-air-temperature oscillations around some initial mean value, we iteratively compute the temperature and compare it with the analytical approximation for a thick and thin debris layers (65 and 23 cm) having thermophysical properties corresponding to the mean of those measured at sites C1 and C2 (Table 1). To explore a range of conditions, including a reversal in the heat flux direction, we also run tests with a variable period of the input heat wave (24–72 hr) and its amplitude (5–10 °C). Figure B1 shows that there is a reasonable agreement between the two methods after the FDM model spin-up time interval, which gets longer with a longer wave period. Furthermore, the scale of observed surface temperature variations is about 2–3 orders of magnitude larger than the difference between the analytical and FDM solutions. Considering that assumptions within rheological models and their parameters make the major impact on our interpretations, and that establishment of the most realistic temperature profiles is not the scope of the paper, we find that the errors of the analytical approximation are acceptable at this stage. Furthermore, contrary to the FDM solution, it is practically useful as it allows to evaluate wave attenuation through the debris mantle depending on its frequency.

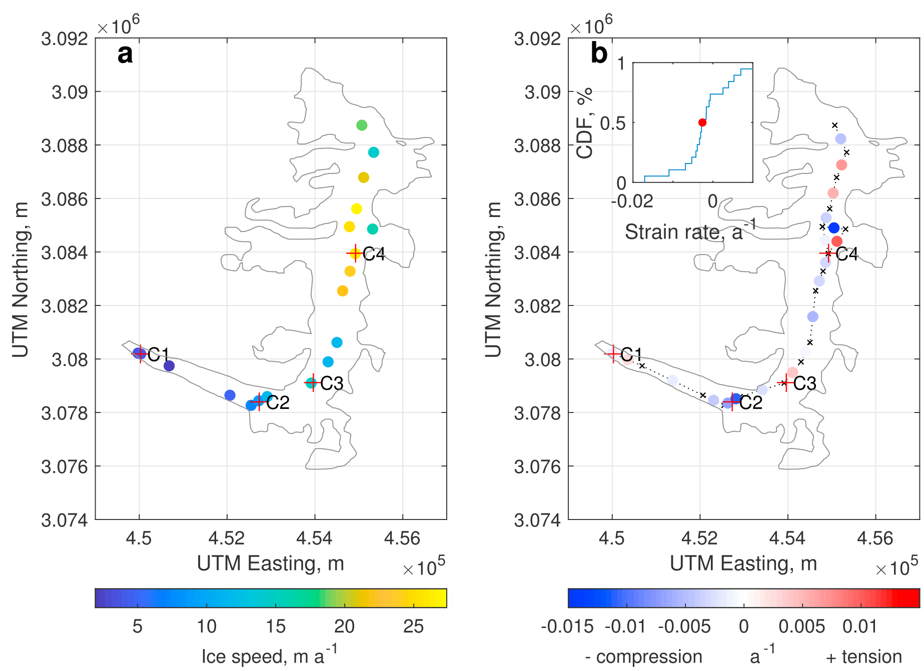

Figure C1. (a) Annual ice speed (2016–2017) derived from a network of global positioning system reference stakes. The red crosses indicate the seismic station positions. (b) Annual strain rates between the nearest stake pairs. The corresponding empirical CDF is shown in the inset, with the median compressive strain rate of 0.0026 a^{-1} indicated by the red dot. Glaciers' outline is adopted from Nuimura et al. (2015). CDF = cumulative distribution function.

Appendix C: Ice Speed and Strain Rates

The measured 2016–2017 ice speeds, derived from a dense network of 19 georeferenced stakes drilled into the glacier, are shown in Figure C1a. The glacier generally decelerates from the highest elevations in the northeast to the lowest elevations in the southwest. The associated annual strain rates ($\dot{\epsilon} = \mathrm{d}V/\mathrm{d}x$) and their statistics are presented in Figure C1b. The median longitudinal strain rates of the glacier are compressive, with a median strain rate of -2.6×10^{-3} a^{-1} and noticeable heterogeneity across the glacier. However, the nearest available strains suggest a compressive regime at each seismic station, with the exception of C3 ($+4\times 10^{-3}$ a^{-1}), although its observed behaviour is not significantly different from the C2 and C4 observations.

The transverse component of the strain rate, $\dot{\epsilon_2}$, is poorly constrained by the network of reference stakes (Figure C1b). The only three measurements that could be considered perpendicular to ice flow are all compressive, with a magnitude ranging from -7×10^{-3} to -17×10^{-3} a^{-1}. We omit the transverse component, $\dot{\epsilon_2}$, from the detailed analysis due to the limited constrains along the glacier and the fact that any additional compressive stress could only slightly suppress the possibility of thermal contraction.

Appendix D: Testing Ice Rheology Models

Figure D1 shows the thermal stresses at the ice surface computed for a simple sine variation of the temperature

$$T(t) = 3.5 \sin(2\pi t) - T_o, \tag{D1}$$

where T_o is between −5 and −35 °C, using four different models: (1) thermoelastic, (2) thermoviscous, and (3 and 4) two Maxwellian thermoviscoelastic models (noncalibrated and calibrated). The first model is a straightforward function of the temperature change in equation (11), the second model is solved by using the analytical expression of equation (10), and the third class of models (equations (12) and (13)) is solved numerically (Matlab ODE45). The following features become immediately apparent:

1. The thermoelastic model is perfectly in phase with the temperature variation and yields the highest stresses at the peak temperatures, which either almost (−5 °C) or sufficiently (−25 °C) reach the tensile fracture strength of ice. Such high stresses seem unrealistic since they imply that ice cracking would commonly occur every night at very modest surface temperatures in terms of their amplitude and the mean. However, this has not been observed to date, as our study, to our knowledge, deals with an exception rather than the norm.
2. The thermoviscous model yields significantly smaller stresses that are in phase with the air temperature change ($\mathrm{d}T/\mathrm{d}t$), and therefore, 90° out of phase with the air temperature (i.e., viscous stresses caused by temperature oscillations are always 0 at the lowest or highest temperatures). The modeled stresses are smaller than the tensile strength of ice. However, the stresses easily reach the critical stress thresholds for crevasse formation (100–400 kPa) for the given conservative conditions of a "warm" case, whereas they approach the tensile strength of ice for a "cold" case (Figure D1).
   Even if the aforementioned instantaneous temperature dependency of creep is introduced ($T_o = T(t)$), it cannot provide an overall stress phase delay, and only leads to a slightly higher stress amplitude at colder temperatures. The latter feature is expressed in Figure D1 as an asymmetry around the points where $T(t) = T_o$. Interestingly, this effect becomes strong enough at low temperatures of the cold case (Figure D1b) that it can lead to stresses close to the tensile strength of ice. It therefore appears that the purely viscous model is not the most realistic model, based on our previous arguments regarding the elastic response and the fact that the strongest seismic signal, which is associated with thermal cracking, is correlated with the air temperature but not its derivative (Podolskiy et al., 2018b).
3. The hybrid thermoviscoelastic model with the Glen-Nye law (equations (12)) shows results similar to the warm case of the thermoviscous model (Figure D1a). This is so due to the efficient viscous relaxation of any accumulated stresses at relatively warm temperatures. However, the stress cannot be rapidly relaxed as the mean temperature decreases, due to the higher viscosity of ice at cold temperatures (Figure D1b). This means that the stress amplitude and phase will be shifted toward the purely elastic response at colder temperatures (i.e., when the absolute stress changes almost in phase with the temperature).
   However, the overall viscoelastic behaviour is sensitive to both the surface temperature and the Young's modulus of ice, as shown in Figure D1c. This figure explores the sensitivity of equation (12) to 24 different

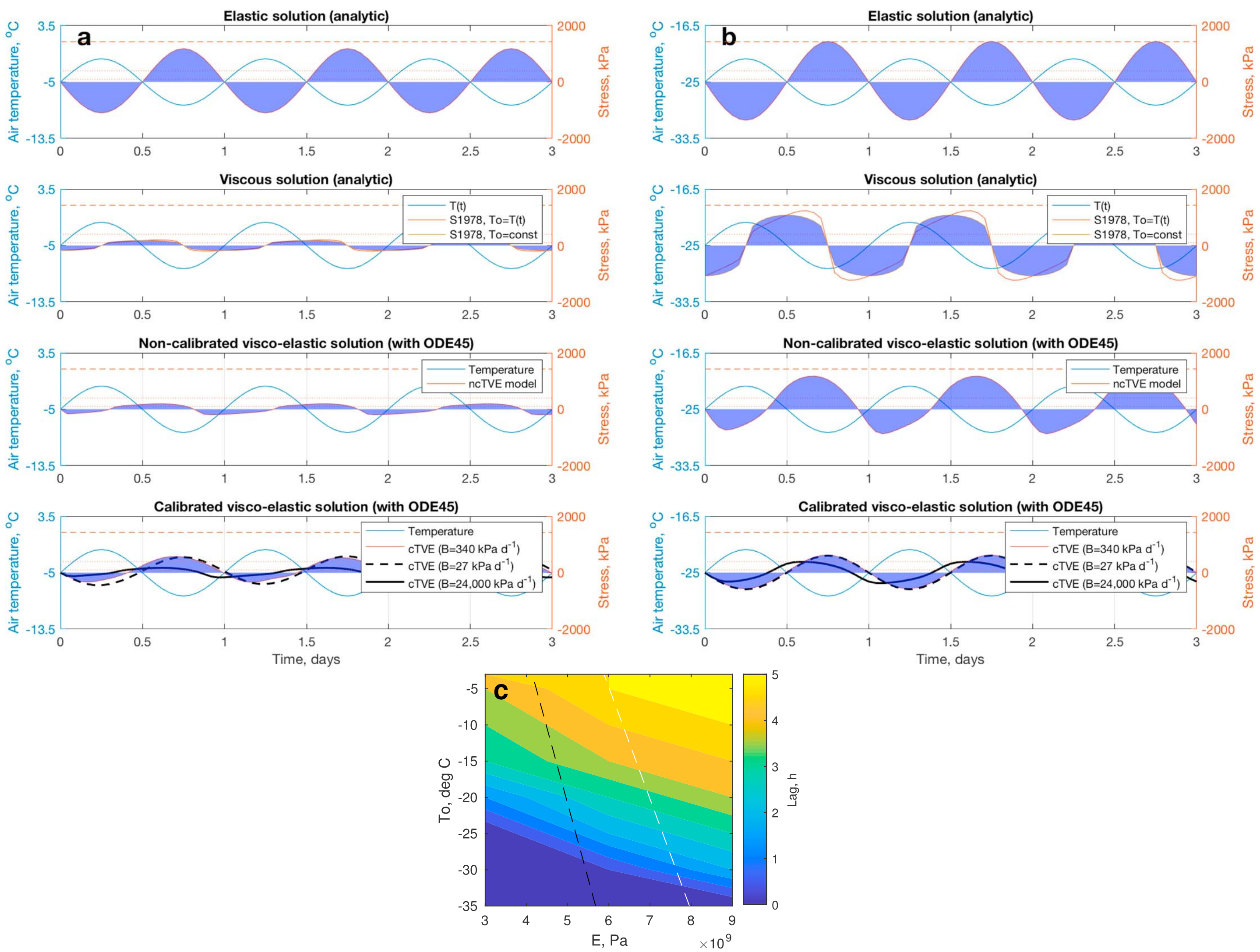

Figure D1. Comparison of the different rheological models for (a) warm (−5 °C) and (b) cold (−25 °C) mean surface temperatures. The dashed and dotted lines show the tensile strength of ice and the critical stress range for crevasse formation, respectively (after Colgan et al., 2016; Petrovic, 2003). (c) Transition between viscous-dominant and elastic-dominant behavior for different Young's modulus (E) and temperature (To) values in the viscoelastic model using Glen-Nye rheology. Colors represent a lag (in hours) measured by cross-correlation of the temperature and the stress. The dashed white line represents Young's modulus as a function of To (see Mellon, 1997, and references within). The dashed black line represents the same relationship, but for low strain rates (see Petrich et al., 2015, and references within).

combinations of the temperature and the Young's modulus of ice; specifically, it covers a parameter space corresponding to [3, 6, 9] GPa $\times[-35, -30, -25, -20, -15, -10, -5, -3]$ °C. It appears that softer ice (i.e., with initially low value of the Young's modulus, e.g., 3 GPa) can shift the stress phase toward a more elastic response (by reducing a time lag between the temperature and the stress), and vice versa, more rigid ice can shift the stress phase toward a more viscous response (by increasing a time lag between the temperature and the stress). This seemingly contradictory response is due to the nonlinear behavior of the stress equation (equation (12)), as explained below.

The above-mentioned features can generally be interpreted as follows. The temperature dependence of the creep factor (i.e., Arrhenius relationship) controls the viscous stress relaxation, which corresponds to a decreasing ice viscosity as the temperature increases. Therefore, a slower creep cannot keep pace with the increasing stress as the temperature decreases, leading to higher stresses and a more elastic response. At the same time, a high Young's modulus during cold conditions (e.g., ice with a high effective viscosity), corresponds to higher stresses. However, the lag between the temperature and stress is reduced as the ice is softened (Figure D1c). This interesting behavior stems from a nonlinear balance between viscous relaxation and the elastic stress rate. Stiffer ice undergoes a nearly instantaneous activation of creep from a large-amplitude thermal wave, whereas softer ice can "absorb" the rapid thermal deformation, which is later relaxed.

4. Finally, the calibrated thermoviscoelastic model of Petrich et al. (2015) shows that an "elastic" response can be observed using B values between 27 and 340 kPa/day, even at relatively warm temperatures, and that the elastic-stress amplitude is significantly relaxed by the creep (Figure D1). A significantly larger B value of 24,000 kPa/day yields a more viscous response, which is similar to performance of all other models with viscous components, but only in the warm case. In the cold case, the hybrid thermoviscoelastic model with the Glen-Nye law gives higher stresses, which are still not completely in phase with temperature oscillations. Furthermore, as demonstrated by our analysis in the main text, the pure elastic model can not relax any long-term accumulated stress, while the calibrated model can.

It can therefore be seen that the most realistic model is the one that implements a thermoelastoviscous ice rheology. However, the model with the Glen-Nye flow law does not allow for the elastic timing of stresses (i.e., which is in phase with temperature) if we assume ice parameters that are typical for warm and "rigid" ice. We have found that it is necessary to use a relatively cold mean surface temperature to avoid the rapid relaxation of elastic stress in our corresponding tests. This constraint simply translates to an increase in the effective viscosity of ice via less creep.

It is important to recognize that a calibration of the Glen-Nye flow law parameters using laboratory experiments and terrestrial ice dynamics models has been a debated topic for decades (e.g., Cuffey & Paterson, 2010; Greve & Blatter, 2009). However, different creep exponents are used in different scientific communities (e.g., $n = 3$ is typical for terrestrial glaciers, but $n = 4$ is common in planetary studies; Mellon, 1997), despite years of research. This highlights that it is not straightforward to adopt values from the glaciological literature for our focused analysis of near-surface ice dynamics. We therefore find it most appropriate to adopt the calibrated viscoelastic empirical approach of Petrich et al. (2015) instead of the non-calibrated viscoelastic model based on the Glen-Nye flow law (equation (10)), since we could not find any parameters that were validated against measured thermal stresses in glacial ice.

Finally, it is necessary to consider Young's modulus for the near-surface ice. According to a review by Mellon (1997), Young's modulus is inversely related to temperature:

$$E(T) = 2.339 \times 10^{10} - 6.48 \times 10^{7}(To + 273.15), \tag{D2}$$

where T is temperature in °C, which yields E ~5.7 GPa for a temperature of ~0 °C (see Figure D1). It is reasonable to assume that this is at the higher end of the modulus range, given the long history of weathering, fracturing, and advection of the near-surface ice and that a lower effective stiffness should be expected. To our knowledge, there are no mechanical tests on near-surface ice that provide a reference. However, it is also important to take into account the dependence of Young's modulus on strain rates, which are relatively low ($\sim 10^{-8}$ s^{-1}). According to Petrich et al. (2015) and references within, the temperature dependence of Young's modulus at low strain rates is as follows:

$$E(T) = E_o(1 - CT), \tag{D3}$$

where $E_o = 4$ GPa and C = 0.012 ° C^{-1}.

At temperature of −5 °C, Mellon (1997) and Petrich et al. (2015) approaches lead to Young's modulus of approximately 4.2 and 6.0 GPa, respectively, which is consistent with a constant value of 5 GPa used by MacAyeal et al. (2019) for estimating diurnal thermal bending moment of an ice plate.

Acknowledgments
We thank F. Walter for encouragement to develop the presented model, A. Tsushima and R. B. Kayastha for logistical support during the field campaign in 2017, S. Sugiyama for sharing his teaching materials about FDM, and D. Sakakibara for his help with cartography plots. Discussions with R. Greve and K. Hutter greatly improved the paper. We also thank S. Westermann and the two anonymous reviewers for their thoughtful comments. This study was supported by Japan Society for the Promotion of Science Grant grants 26257202, 17H1621, 18K18175, 18KK0098. The signal processing and figure production were done using the ObsPy, QGIS, and Matlab technical languages. The original data discussed in the paper are described by Podolskiy et al. (2018b), and are freely available (Podolskiy et al., 2018a).

References

Andreotti, B., Forterre, Y., & Pouliquen, O. (2013). *Granular media*. Cambridge, UK: Cambridge University Press.

Attree, N., Groussin, O., Jorda, L., Rodionov, S., Auger, A. T., Thomas, N., & Hartogh, P. (2017). Thermal fracturing on comets. Applications to 67P/Churyumov-Gerasimenko. *Astronomy & Astrophysics*, *610*, A76. https://doi.org/10.1051/0004-6361/201731937

Bazant, Z. P. (1992). Large-scale thermal bending fracture of sea ice plates. *Journal of Geophysical Research*, *97*(C11), 17,739–17,751. https://doi.org/10.1029/92JC00816

Ben-Zion, Y., & Leary, P. (1986). Thermoelastic strain in a half-space covered by unconsolidated material. *BSSA*, *76*(5), 1447–1460.

Berger, J. (1975). A note on thermoelastic strains and tilts. *Journal of Geophysical Research*, *80*(2), 274–277. https://doi.org/10.1029/JB080i002p00274

Browning, J., Meredith, P., & Gudmundsson, A. (2016). Cooling-dominated cracking in thermally stressed volcanic rocks. *Geophysical Research Letters*, *43*, 8417–8425. https://doi.org/10.1002/2016GL070532

Carmichael, J. D., Pettit, E. C., Hoffman, M., Fountain, A., & Hallet, B. (2012). Seismic multiplet response triggered by melt at Blood Falls, Taylor Glacier, Antarctica. *Journal of Geophysical Research*, *117*, F03004. https://doi.org/10.1029/2011JF002221

Carr, E. J., & March, N. G. (2018). Semi-analytical solution of multilayer diffusion problems with time-varying boundary conditions and general interface conditions. *Applied Mathematics and Computation*, *333*, 286–303. https://doi.org/https://doi.org/10.1016/j.amc.2018.03.095

Christmann, J., Müller, R., & Humbert, A. (2019). On nonlinear strain theory for a viscoelastic material model and its implications for calving of ice shelves. *Journal of Glaciology*, *65*(250), 212–224. https://doi.org/10.1017/jog.2018.107

Colgan, W., Rajaram, H., Abdalati, W., McCutchan, C., Mottram, R., Moussavi, M. S., & Grigsby, S. (2016). Glacier crevasses: Observations, models, and mass balance implications. *Reviews of Geophysics*, *54*, 119–161. https://doi.org/10.1002/2015RG000504

Cook, J. M., Hodson, A. J., & Irvine-Fynn, T. D. L. (2016). Supraglacial weathering crust dynamics inferred from cryoconite hole hydrology. *Hydrological Processes*, *30*(3), 433–446. https://doi.org/10.1002/hyp.10602

Cooper, M. G., Smith, L. C., Rennermalm, A. K., Miège, C., Pitcher, L. H., Ryan, J. C., & Cooley, S. W. (2018). Meltwater storage in low-density near-surface bare ice in the Greenland ice sheet ablation zone. *The Cryosphere*, *12*(3), 955–970. https://doi.org/10.5194/tc-12-955-2018

Cuffey, K., & Paterson, W. (2010). *The physics of glaciers* (4th ed.). Amsterdam, Netherlands: Academic Press.

Evans, R. J., & Untersteiner, N. (1971). Thermal cracks in floating ice sheets. *Journal of Geophysical Research*, *76*(3), 694–703. https://doi.org/10.1029/JC076i003p00694

Ferrari, C. (2018). Thermal properties of icy surfaces in the outer solar system. *Space Science Reviews*, *214*(8), 111. https://doi.org/10.1007/s11214-018-0546-x

Fujita, K., & Sakai, A. (2014). Modelling runoff from a Himalayan debris-covered glacier. *HESS*, *18*(7), 2679–2694. https://doi.org/10.5194/hess-18-2679-2014

Girard, L., Bouillon, S., Weiss, J., Amitrano, D., Fichefet, T., & Legat, V. (2011). A new modeling framework for sea-ice mechanics based on elasto-brittle rheology. *Annals of Glaciology*, *52*(57), 123–132. https://doi.org/10.3189/172756411795931499

González de la Cruz, G., & Gurevich, Y. G. (1995). Thermal diffusion of a two-layer system. *Physical Review B*, *51*, 2188–2192. https://doi.org/10.1103/PhysRevB.51.2188

Greve, R., & Blatter, H. (2009). *Dynamics of ice sheets and glaciers*. Berlin, Germany: Springer.

Hickson, R., Barry, S., Mercer, G., & Sidhu, H. (2011). Finite difference schemes for multilayer diffusion. *Mathematical and Computer Modelling*, *54*(1), 210–220. https://doi.org/https://doi.org/10.1016/j.mcm.2011.02.003

Hoffman, M. J., Fountain, A. G., & Liston, G. E. (2014). Near-surface internal melting: A substantial mass loss on Antarctic Dry Valley glaciers. *Journal of Glaciology*, *60*(220), 361–374. https://doi.org/10.3189/2014JoG13J095

Jafarov, E. E., Marchenko, S. S., & Romanovsky, V. E. (2012). Numerical modeling of permafrost dynamics in Alaska using a high spatial resolution dataset. *The Cryosphere*, *6*(3), 613–624. https://doi.org/10.5194/tc-6-613-2012

Jia, X., Laurent, J., Khidas, Y., & Langlois, V. (2009). Sound scattering in dense granular media. *Chinese Science Bulletin*, *54*(23), 4327–4336. https://doi.org/10.1007/s11434-009-0609-1

Keller, A., & Hutter, K. (2014). A viscoelastic damage model for polycrystalline ice, inspired by Weibull-distributed fiber bundle models. Part I: Constitutive models. *Continuum Mechanics and Thermodynamics*, *26*(6), 879–894. https://doi.org/10.1007/s00161-014-0348-7

Krug, J., Weiss, J., Gagliardini, O., & Durand, G. (2014). Combining damage and fracture mechanics to model calving. *The Cryosphere*, *8*(6), 2101–2117. https://doi.org/10.5194/tc-8-2101-2014

Lachenbruch, A. (1962). Mechanics of thermal contraction cracks and ice wedge polygons in permafrost. *Special Paper of the Geological Society of America*, *70*, 69.

Levy, J., Head, J., & Marchant, D. (2009). Thermal contraction crack polygons on Mars: Classification, distribution, and climate implications from HiRISE observations. *Journal of Geophysical Research*, *114*, E01007. https://doi.org/10.1029/2008JE003273

Lewis, J. K. (1993). A model for thermally-induced stresses in multi-year sea ice. *Cold Regions Science and Technology*, *21*(4), 337–348. https://doi.org/10.1016/0165-232X(93)90011-V

Lewis, J. K. (1994). Relating Arctic ambient noise to thermally induced fracturing of the ice pack. *The Journal of the Acoustical Society of America*, *95*(3), 1378–1385. https://doi.org/10.1121/1.408576

MacAyeal, D. R., Banwell, A. F., Okal, E. A., Lin, J., Willis, I. C., Goodsell, B., & MacDonald, G. J. (2019). Diurnal seismicity cycle linked to subsurface melting on an ice shelf. *Annals of Glaciology*, *60*(79), 1–21. https://doi.org/10.1017/aog.2018.29

Marchant, D., Lewis, A., Phillips, W., Moore, E., Souchez, R., Denton, G., & Landis, G. (2002). Formation of patterned ground and sublimation till over Miocene glacier ice in Beacon Valley, southern Victoria Land, Antarctica. *GSA Bulletin*, *114*(6), 718. https://doi.org/10.1130/0016-7606(2002)114<0718:FOPGAS>2.0.CO;2

Matsuoka, N., Christiansen, H. H., & Watanabe, T. (2018). Ice-wedge polygon dynamics in Svalbard: Lessons from a decade of automated multi-sensor monitoring. *Permafrost and Periglacial Processes*, *29*(3), 210–227. https://doi.org/10.1002/ppp.1985

Mellon, M. (1997). Small-scale polygonal features on Mars: Seasonal thermal contraction cracks in permafrost. *Journal of Geophysical Research*, *102*(E11), 25,617–25,628. https://doi.org/10.1029/97JE02582

Milne, A. R., Ganton, J. H., & McMillin, D. J. (1967). Ambient noise under sea ice and further measurements of wind and temperature dependence. *The Journal of the Acoustical Society of America*, *41*(2), 525–528. https://doi.org/10.1121/1.1910367

Nansen, F. (1897). *Farthest north, Vol. II*. New York: Harper & Brothers Publishers.

Neave, K., & Savage, J. (1970). Icequakes on the Athabasca Glacier. *Journal of Geophysical Research*, *75*(8), 1351–1362.

Nicholson, L., & Benn, D. I. (2006). Calculating ice melt beneath a debris layer using meteorological data. *Journal of Glaciology*, *52*(178), 463–470. https://doi.org/10.3189/172756506781828584

Nishio, F. (1983). Thermally induced fractures and snowquakes of polar snow cover. *Memoirs of National Institute of Polar Research. Series C*, *14*, 1–48.

Nuimura, T., Sakai, A., Taniguchi, K., Nagai, H., Lamsal, D., Tsutaki, S., & Fujita, K. (2015). The GAMDAM glacier inventory: A quality-controlled inventory of Asian glaciers. *Cryosphere*, *9*(3), 849–864. https://doi.org/10.5194/tc-9-849-2015

O'Neill, H. B., & Christiansen, H. H. (2018). Detection of ice wedge cracking in permafrost using miniature accelerometers. *Journal of Geophysical Research: Earth Surface*, *123*, 642–657. https://doi.org/10.1002/2017JF004343

Petrich, C., Saether, I., Fransson, L., Sand, B., & Arntsen, B. (2015). Time-dependent spatial distribution of thermal stresses in the ice cover of a small reservoir. *Cold Regions Science and Technology*, *120*, 35–44. https://doi.org/10.1016/j.coldregions.2015.09.003

Petrovic, J. J. (2003). Review Mechanical properties of ice and snow. *Journal of Materials Science*, *38*(1), 1–6. https://doi.org/10.1023/A:1021134128038

Podolskiy, E., Fujita, K., Sunako, S., Tsushima, A., & Kayastha, R. (2018a). Seismic and meteorological records from Trakarding-Trambau Glacier system, Nepal Himalaya (October 21 - November 9, 2017), Zenodo https://doi.org/10.5281/zenodo.1323475

Podolskiy, E. A., Fujita, K., Sunako, S., Tsushima, A., & Kayastha, R. B. (2018b). Nocturnal thermal fracturing of a Himalayan debris-covered glacier revealed by ambient seismic noise. *Geophysical Research Letters*, *45*, 9699–9709. https://doi.org/10.1029/2018GL079653

Podolskiy, E., Lobkina, V., Gensiorovsky, Y., & Thibert, E. (2015). Evaluating ablation and environmental impact of giant anthropogenic snow patches (Yuzhno-Sakhalinsk, Russia). *Cold Regions Science and Technology*, *114*, 44–60. https://doi.org/10.1016/j.coldregions.2015.03.001

Podolskiy, E. A., & Walter, F. (2016). Cryoseismology. *Reviews of Geophysics*, *54*, 708–758. https://doi.org/10.1002/2016RG000526

Pralong, A., & Funk, M. (2005). Dynamic damage model of crevasse opening and application to glacier calving. *Journal of Geophysical Research*, *110*, B01309. https://doi.org/10.1029/2004JB003104

Prawirodirdjo, L., Ben-Zion, Y., & Bock, Y. (2006). Observation and modeling of thermoelastic strain in Southern California Integrated GPS Network daily position time series. *Journal of Geophysical Research*, *111*, B02408. https://doi.org/10.1029/2005JB003716

Reid, T. D., & Brock, B. W. (2010). An energy-balance model for debris-covered glaciers including heat conduction through the debris layer. *Journal of Glaciology*, *56*(199), 903–916. https://doi.org/10.3189/002214310794457218

Richter, T., Sens-Schönfelder, C., Kind, R., & Asch, G. (2014). Comprehensive observation and modeling of earthquake and temperature-related seismic velocity changes in northern Chile with passive image interferometry. *Journal of Geophysical Research: Solid Earth*, *119*, 4747–4765. https://doi.org/10.1002/2013JB010695

Riesen, P., Hutter, K., & Funk, M. (2010). A viscoelastic Rivlin-Ericksen material model applicable to glacier ice. *Nonlinear Processes in Geophysics*, *17*(6), 673–684. https://doi.org/10.5194/npg-17-673-2010

Röösli, C., Walter, F., Husen, S., Andrews, L. C., Lüthi, M. P., Catania, G. A., & Kissling, E. (2014). Sustained seismic tremors and icequakes detected in the ablation zone of the Greenland ice sheet. *Journal of Glaciology*, *60*(221), 563–575. https://doi.org/10.3189/2014JoG13J210

Sanderson, T. J. O. (1978). Thermal stresses near the surface of a glacier. *Journal of Glaciology*, *20*(83), 257–283. https://doi.org/10.3189/S0022143000013836

van der Veen, C. (1998). Fracture mechanics approach to penetration of surface crevasses on glaciers. *Cold Regions Science and Technology*, *27*(1), 31–47. https://doi.org/10.1016/S0165-232X(97)00022-0

Xie, Y., & Farmer, D. M. (1991). Acoustical radiation from thermally stressed sea ice. *The Journal of the Acoustical Society of America*, *89*(5), 2215–2231. https://doi.org/10.1121/1.400914

Zhang, T., Chen, Y., Ding, M., Shen, Z., Yang, Y., & Guan, Q. (2019). Air-temperature control on diurnal variations in microseismicity at Laohugou Glacier No. 12, Qilian Mountains. *Annals of Glaciology*, *60*(79), 1–12. https://doi.org/10.1017/aog.2018.34

Erratum

In the originally published version of this manuscript, a portion of the equation given in the third column of the fourth row of Table 1 was reproduced in the fourth column of the fourth row. This error has been corrected, and this may be considered the authoritative version of record.